

Medical University of South Carolina

MEDICA

MUSC Theses and Dissertations

2015

Extensive and Persistent Disruption of Neurovascular Coupling by a Single Cerebral Microinfarct

Philipp McConnell Summers
Medical University of South Carolina

Follow this and additional works at: <https://medica-musc.researchcommons.org/theses>

Recommended Citation

Summers, Philipp McConnell, "Extensive and Persistent Disruption of Neurovascular Coupling by a Single Cerebral Microinfarct" (2015). *MUSC Theses and Dissertations*. 484.
<https://medica-musc.researchcommons.org/theses/484>

This Thesis is brought to you for free and open access by MEDICA. It has been accepted for inclusion in MUSC Theses and Dissertations by an authorized administrator of MEDICA. For more information, please contact medica@musc.edu.

Extensive and Persistent Disruption of Neurovascular Coupling by a Single
Cerebral Microinfarct by

Philipp Summers

A thesis submitted to the faculty of the Medical University of South Carolina in
partial fulfillment of the requirements for the degree of Master's of Science in
Neurosciences in the College of Graduate Studies

Department of Neurosciences, 2015

Approved by:

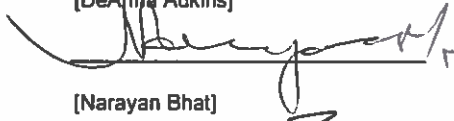
Chairman, Advisory Committee



[Andy Shih]



[DeAnna Adkins]



[Narayan Bhat]



[Truman Brown]



[Prakash Kara]

PHILIPP MCCONNELL SUMMERS. Extensive and Persistent Disruption of Neurovascular Coupling by a Single Cerebral Microinfarct. (Under the direction of Andy Shih).

Abstract

Cerebral microinfarcts (CMI), microscopic brain lesions caused by blockade of small blood vessels, have recently emerged as a potential determinant of cognitive decline. Though small in size, our recent work demonstrated that a single, strategically placed CMI was sufficient to disrupt sensory input in a behavioral task. However, the means by which such small lesions disrupt brain function remain poorly understood. We imaged vascular function in awake, head-fixed mice using two-photon microscopy to examine the impact of CMI on neurovascular coupling. CMI were generated in cortex by photothrombotic occlusion of single penetrating vessels through a thinned-skull cranial window. Vibrissa-evoked dilation of individual arteries and arterioles within the primary vibrissa cortex were tracked over four time periods: pre-occlusion, acute (2-3 days post-occlusion), subacute (7-9 days) and chronic (14-21 days). In the acute phase, dilatory responses were markedly attenuated compared to pre-occlusion ($2.2 \pm 0.5\%$ mean dilation over baseline vs. $11.2 \pm 0.8\%$, $p < 0.001$). Dilatory responses during the subacute ($7.8 \pm 1.1\%$) and chronic ($6.5 \pm 1.1\%$) phases partially recovered but remained significantly attenuated in magnitude and time to dilation compared to pre-occlusion ($p < 0.01$). Critically, vascular dysfunction was observed well beyond the borders of the CMI, as infarcts with an average radius of 0.19 ± 0.05 mm generated deficits in dilation at distances exceeding 1 mm away from the vessel targeted for occlusion. Analysis of dilations in a separate cohort of mice during the hyperacute time period (0-3 hours post-occlusion), revealed that the dilatory deficit is first expressed in the immediate vicinity of the stroke and then propagates outward from the occlusion site. While unresponsive to sensory stimulation, vasodilation could be evoked by isoflurane inhalation, albeit attenuated in the subacute phase ($156.7 \pm 5.3\%$ of pre-stroke levels vs. $134.6 \pm 4.3\%$ subacute, $p = 0.02$). Expression of c-Fos following an extended period of vibrissa stimulation was reduced in the peri-infarct tissue in the acute time period, with gradual recovery initiating distal to the stroke apparent in subacute and chronic mice. This indicated that loss of sensory-evoked vasodilation is attributed to a combination of altered vascular mechanical properties and a deficit in neural connectivity and/or activity. Thus, CMI disrupt brain function well beyond the regions of overt tissue infarction and this effect, combined with their widespread distribution in the aged brain, may contribute to the pathogenesis of CMI in vascular dementia.

Contents

Abstract	ii
Contents	iii
List of Figures	v
List of Abbreviations	vi
Introduction	1
<i>Vasculature of the Brain</i>	1
Neurovascular Coupling	2
The Neurovascular Unit.....	3
2-Photon Imaging as a Tool to Study Neurovascular Coupling	4
<i>Stroke</i>	5
The Ischemic Cascade	5
Effects of Anesthetics on Stroke	8
Cerebral Microinfarcts	10
Targeted Photothrombotic Occlusion.....	11
Methods	12
<i>Subjects</i>	12
<i>Study Design</i>	12
<i>Surgical Procedure – Head Mount Implantation</i>	13
<i>Habituation to Head Fixation</i>	14
<i>Surgical Procedure – PoRTS Window Surgery</i>	15
<i>Imaging Setup</i>	16
<i>Imaging/Stimulation Procedure</i>	19
<i>Photothrombotic Stroke</i>	22
<i>Data Processing</i>	23
<i>Immunohistochemistry</i>	27
<i>c-Fos Immunohistochemistry</i>	28
Results	30
<i>Sensory-Evoked Arteriole Dilatory Response in Awake Mice</i>	30
<i>Cerebral Microinfarcts were targeted to the Periphery of the Barrel Cortex</i>	32

<i>Changes in Dilatory Response Following Cerebral Microinfarct.....</i>	<i>34</i>
<i>Correlations between Changes in Dilatory Response and Position Relative to CMI ...</i>	<i>38</i>
<i>Genesis of a Deficit – Neurovascular Coupling in Hyper-Acute Stage of Cerebral Microinfarction</i>	<i>42</i>
<i>Isoflurane and c-Fos – Tools to Probe the Mechanisms of the Loss of Dilatory Response</i>	<i>44</i>
Discussion.....	50
References.....	58

List of Figures

Figure 1. Vasculature of the mouse cortex.	1
Figure 2. Timeline of experimental procedures	12
Figure 3. Schematic of PoRTS window for imaging mouse cortex.	16
Figure 4. Schematic of Imaging Setup.	18
Figure 5. Stimulation Paradigm and Example of Dilation.	21
Figure 6. Schematic of Targeted Photothrombotic Occlusion of an Arteriole.	23
Figure 7. Example of Full-Width Half-Maximum Measurements of Dilating Arterioles.	24
Figure 8. Vibrissa Stimulation Elicited Robust Dilation in Arterioles within the Vibrissa Cortex.	26
Figure 9. Average Responses of Arterioles and Venules to Stimulation under Basal Conditions.	31
Figure 10. Maximum Dilatory Responses of Individual Arterioles to Stimulation under Basal Conditions.	32
Figure 11. Locations of Imaging Regions and Cerebral Microinfarcts Within the Barrel Cortex	33
Figure 12. Average Dilatory Response of Arterioles Before and Following Occlusion.	34
Figure 13. Mean Latency of Dilation is Augmented in the Acute and Subacute Time Periods.	36
Figure 14. Loss of Dilatory Response in the Acute Time Phase effects both Small and Large Vessels.	37
Figure 15. Loss of dilatory response extended far beyond the CMI border during the acute time phase.	39
Figure 16. Both proximal and distal vessels experienced increase in latency to dilation following stroke.	41
Figure 17: Neurovascular Coupling is Disrupted Proximal to Stroke in the Hyperacute phase.	43
Figure 18. Isoflurane is capable of inducing far larger dilations than vibrissa stimulation.	45
Figure 19. Dilations induced by isoflurane exposure were significantly attenuated in the acute phase, but still greatly exceeded the dilatory response to vibrissa stimulation.	46
Figure 20. Immunofluorescence staining of c-Fos reveals robust neuronal activation in the barrel cortex contralateral to vibrissa stimulation in a sham animal.	47
Figure 21. c-Fos activation in the barrel cortex contralateral to vibrissa stimulation is diminished in the acute phase following CMI.	48
Figure 22. Expression of c-Fos is attenuated proximal to the CMI in the acute and subacute phases.	49

List of Abbreviations

AIS: Axon Initial Segment

ATP: Adenosine Triphosphate

BBB: Blood-Brain Barrier

BOLD: Blood-Oxygenation Level Dependent

CMI: Cerebral Microinfarct

CSD: Cortical Spreading Depression

fMRI: Functional Magnetic Resonance Imaging

NVU: Neurovascular Unit

ROS: Reactive Oxygen Species

TPLSM: Two-Photon Laser-Scanning Microscopy

Introduction

Vasculature of the Brain

The constant energy demands of brain function must be supplied by a reliable and dynamic cerebrovascular system (1). The cerebral cortex is supplied by the great cerebral arteries that emanate from the Circle of Willis and source a planar network of highly interconnected pial arterioles on the brain surface (2). Blood flow in this network is relatively insensitive to blockages (3, 4), and also permits the dynamic redistribution of blood toward regions of heightened electrical activity (5,6).

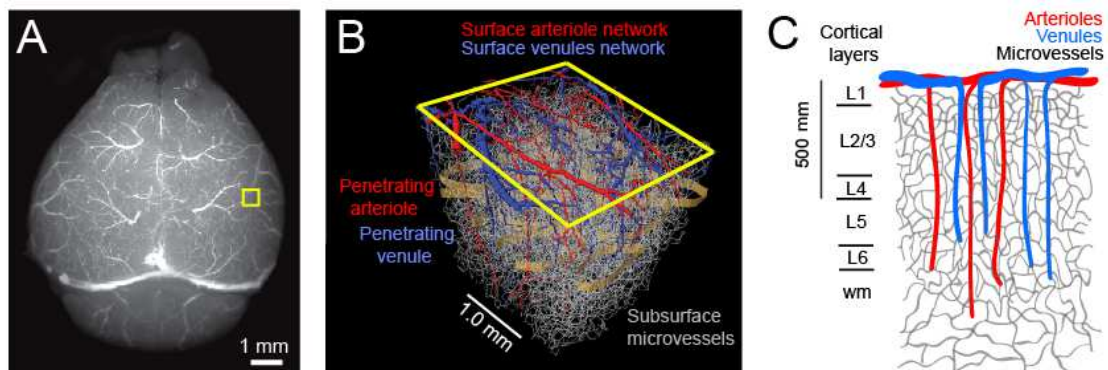


Figure 1. Vasculature of the mouse cortex.

(A) Vasculature of the dorsal surface of the whole mouse brain revealed by a fluorescein-gelatin cast. (B) Schematic of the three-tiered topology of vasculature in the mouse cortex, containing highly interconnected surface pial networks, penetrating vessels which create bottlenecks in flow, and subsurface microvascular networks. Adapted from Blinder et al. (7). (C) Illustration of penetrating vessels projecting radially from the pial surface into deep layers of the cortex. Adapted from Shih et al. (8).

These pial vessels are in turn connected to an underlying, three-dimensional network of microvessels by penetrating arterioles that project radially

from the surface, as shown in **Figure 1B**, forming bottlenecks in flow to columns of cortical microvasculature (7). Blood is drained from the microvasculature back to the cortical surface through penetrating venules and then emptied into the central sinus.

The physiological demands served by the blood supply of the brain are particularly significant because neurons are more sensitive to oxygen deprivation than other kinds of cells with lower rates of metabolism (9). The brain is also at risk from circulating toxins, and is specifically protected in this respect by the blood-brain barrier. In addition to having a high metabolic rate, neurons obtain virtually all of their nutrition via aerobic metabolism of glucose, making them even more reliant on persistent oxygenation (10). When blood supply is compromised, deprivation of oxygen and glucose may cause transient or permanent damage to brain tissue. Even a brief loss of blood supply can initiate cellular changes which lead to cell death, while a prolonged loss of blood flow leads more directly to death and degeneration of affected cells (9).

Neurovascular Coupling

Cerebral metabolism depends on a constant supply of both glucose and oxygen. A continuous supply of these two energy substrates is maintained by cerebral blood flow (CBF), which delivers glucose and oxygen to neural tissue through the complex web of blood vessels in the brain's vascular system.

Accordingly, during neural activity, increases in oxygen and glucose consumption are followed by an increase in CBF (11). While the increase in CBF is comparable to the rise in glucose consumption rate, the rate of oxygen consumption is fractionally smaller in magnitude, resulting in an increase in the relative concentration of oxygen in blood and tissue (12). This oversupply of oxygen due to the mismatch between CBF and oxygen consumption is the basis of blood-oxygenation level dependent (BOLD) fMRI, which detects alterations in levels of deoxygenated hemoglobin and cerebral blood volume (13, 14).

The Neurovascular Unit

Neurovascular coupling is accomplished through the activity of a group of cells, closely related to each other, called the neurovascular unit (NVU). The NVU is composed of neurons, astrocytes, endothelial cells of the blood-brain barrier (BBB), myocytes, and pericytes (15). These components exhibit a tightly linked anatomical and chemical relationship that detects neuronal metabolic needs and triggers the necessary vasodilatory or vasoconstrictive response needed to regulate nutrient distribution and meet such demands. The NVU has also been implicated in eliciting selective changes in BBB permeability, either through direct signaling from neurons or alternative pathways through pericytes and astrocytes which ensheath the microvasculature (15, 16).

2-Photon Imaging as a Tool to Study Neurovascular Coupling

Two-photon laser-scanning microscopy (TPLSM) is an imaging technique which combines the point-by-point rastering technique of confocal laser scanning microscopy with physical phenomena of two-photon absorption, which is the simultaneous absorption of two photons to excite a molecule from one state to a higher energy electronic state (17). As a result of this phenomenon, the two excitation photons can provide the excitation of a photon with twice their own energy. Many fluorescent markers used in in-vivo imaging require excitation light in the visible spectrum, which is scattered at relatively shallow depths in brain tissue. Two-photon microscopy allows researchers to circumvent these issues by providing excitation for the same fluorophores from the infra-red spectrum by way of two-photon absorption, permitting greater depth of imaging with less scattering of excitation light (18).

The depth of imaging allowed by two-photon microscopy, combined with the high spatial-acuity of laser scanning microscopy, make this imaging method one of the most amenable for imaging living tissue up to a very high depth. Due to multiphoton absorption, the background signal is strongly suppressed, resulting in improved light detection efficiency, and reduced phototoxicity compared to confocal microscopy. *In vivo* TPLSM is already an established method to visualize cerebrovascular topology and quantify blood flow at the level of single vessels in the rodent cortex, and is an excellent tool for probing neurovascular coupling at the microvascular level in the behaving animal (8).

Stroke

A stroke is defined as the loss of brain function due to a disturbance in the blood supply to the brain (19). This can arise either from ischemia, a lack of blood flow due to a clot or general hypoxia, or hemorrhage, a loss of blood flow due to rupture of a vessel. The majority of strokes (87%) are ischemic strokes. Every year, about 800,000 people in the United States have a stroke (20). While stroke is the fourth leading cause of death in America, killing nearly 130,000 individuals each year (21), a large proportion of patients survive its devastating effects and require rehabilitation and long-term care to overcome disabilities. As a result, stroke is a great burden to the economy, costing the United States an estimated \$36.5 billion annually (22).

The Ischemic Cascade

The progression of stroke injury is very complex, involving various mechanisms of cell death including excitotoxicity, apoptosis, necrosis and inflammation. Following the loss of blood supply, stroke begins with the disruption of metabolism and homeostasis in neurons and glia due to an inability to generate adequate levels of adenosine triphosphate (ATP) (23). The loss of ATP-dependent ion channel activity results in a breakdown of ionic gradients across the plasma membrane, resulting in widespread depolarization of neurons

and glia and subsequent uncontrolled release of synaptic glutamate (24, 25). The loss of membrane potential also shuts down Na^+ -dependent glutamate transporters, preventing reuptake and further exacerbating extracellular glutamate accumulation (26).

The rise in glutamate initiates a toxic secondary cascade known as excitotoxicity (27, 28). The elevated levels of glutamate over-stimulate NMDA and AMPA-type neuronal glutamate receptors, leading to an influx and accumulation of Ca^{++} in the cytosol (29). Intracellular Ca^{++} overload leads to mitochondrial dysfunction, compounding the issue of ATP depletion and triggering the apoptotic cascade.

Cortical spreading depression (CSD) is an intense depolarization wave that slowly propagates through gray matter. CSD is characterized by a wave of hyperactivity followed by a wave of depression (30), and is associated with massive transmembrane ionic and water shifts coupled to a surge in extracellular K^+ (31). CSD has been found to coincide with tissue hypoxia (32), and incidences of spreading depression, sometimes termed “injury depolarizations”, have been detected in the human brain following ischemic stroke, subarachnoid hemorrhage, intracerebral hemorrhage, and traumatic brain injury (33). In ischemic stroke, spreading depressions seem to originate at the junction between the ischemic core and the moderately ischemic penumbra, where synaptic activity has ceased, but some neuronal membrane potentials are preserved. These depolarizations propagate along the infarct rim and often into

non-ischemic tissue, exerting metabolic and hemodynamic effects that can worsen the long-term outcome of ischemic tissue (34).

In ischemic stroke, the reduction of CBF is most pronounced in the ischemic core, while it is less pronounced in the periphery (35). Following focal and global ischemia, when perfusion is reestablished in the peri-infarct, there is a transient increase in flow followed by a period of reduced flow. After ischemia, cerebral circulation experiences some degree of vasoparalysis (36). It has long been known that, following ischemic stroke, the reactivity of cerebral circulation to administration of carbon dioxide and vascular autoregulation is altered and impaired in patients (37). Studies that assess indices of neural activity in patients suggest that the reduction in neurovascular coupling may be secondary to a reduction in the neural activity driving the hemodynamic response (38). It has also been found that the increase in glucose utilization typically evoked by vibrissa stimulation of rats is severely depressed one day following transient global ischemia (39), indicating that, in addition to a depressed CBF response, metabolic responses are attenuated following stroke. Small cortical strokes have been found to produce a broad region of hypometabolism, termed diaschisis, outside of the putative ischemic core (40). It is postulated that this is due to vascular steal (41), or the loss of the CBF to neighboring hypometabolic regions, and a deficit in neural activity resulting from the loss of afferents that previously emerged from the stroke core (42).

CSD may, to some extent, drive these effects, as it has been found to elicit a strong vasoconstrictive response in the peri-infarct tissue (43). Widespread vascular oxidative stress could also contribute to loss of neurovascular coupling. Ischemia leads to an increase of reactive oxygen species (ROS), which can cause profound alterations in cerebrovascular regulation (44), while ROS scavengers ameliorate disturbances in CBF following ischemia-reperfusion (45).

Effects of Anesthetics on Stroke

Anesthesia alters key mechanisms of stroke injury and repair, and will therefore affect the trajectory of the disease. In the acute stage of ischemic injury, this can occur by suppression of neuronal activity or by engaging collateral blood flow sources. Common anesthetics, such as isoflurane, reduce the cerebral metabolic rate for oxygen consumption and likely the extent of excitotoxic neuronal toxicity (46). Ketamine, in particular, is an antagonist of the NMDA receptor and attenuates production of the potent vasomediator, nitric oxide, during stroke (47). The frequency of CSD events has been shown to be attenuated or modulated by numerous anesthetics, including ketamine (48, 49), volatile anesthetics halothane, isoflurane and sevoflurane (50, 51), and urethane-chloralose (52). Thus, many anesthetics mediate an overall protective effect in stroke by attenuating excitotoxic injury (53).

Anesthesia can also affect CBF, which may have opposing effects on stroke outcome. Pentobarbital and isoflurane, in particular, cause global cerebral vasodilation and a significant reduction in CBF that lead to a hypoperfusion (54). In the setting of a stroke, this could conceivably decrease perfusion in the stroke penumbra, exacerbating injury. Conversely, the dilation of cerebral arterioles can conceivably promote tissue survival by engaging collateral blood supply to the hypoxic tissue. Another important consideration is that hemodynamic responses measured by BOLD fMRI are widely used to infer tissue recovery after stroke (55). Given the suppressive effects of anesthetics on arterial and neuronal reactivity, it is unclear when models using anesthesia fail to mimic the human condition (56, 57).

The effects of anesthetics can extend beyond the acute phase of stroke when the infarct stabilizes and the peri-infarct zone begins to recover. Longitudinal *in vivo* imaging studies typically involve repeated periods of anesthesia that could affect repair/recovery processes. Anesthetics impact the activity of microglia directly by altering the expression of inflammatory mediators and also indirectly by reducing CSD, which promotes microglial activation (58). The effect varies with the type of anesthetic used, as isoflurane appears to promote cytokine expression (59, 60), while ketamine has an inhibitory effect (61). Further, the activity of microglia is tightly linked to post-stroke repair process through release of matrix metalloproteinases, which are associated with the breakdown of tight junction proteins in acute stroke (62), but also appear to

be involved in remodeling of neuronal connectivity (63) and possibly nascent blood vessel formation (64).

One limitation in current preclinical stroke studies is that the models are often invasive, necessitating deep and prolonged anesthesia. This precludes the visualization of early changes in stroke, and can dictate the extent and long-term trajectory of the injury. To minimize the confounding influence of anesthetics in this study, mice were imaged and vessels were occluded in the awakened state, with minimal isoflurane exposure introduced briefly to allow for necessary injections.

Cerebral Microinfarcts

Cerebral microinfarcts (CMIs) are tiny lesions characterized by genuine tissue infarction, but on a scale that renders them unapparent in gross pathologic examination or conventional structural MRI, although there is evidence that *in vivo* detection of microinfarcts might soon be possible (65). Though many studies have shown that asymptomatic microinfarcts and cerebrovascular disease are very common, especially with aging, these “silent” strokes are nearly twice as prevalent in cases of dementia as in the healthy, aged brain (66, 67). While the clinical relevance of CMIs has been controversial, there is a growing body of evidence that they impart a deleterious effect on cognitive performance. In a study where CMIs were introduced in the rat barrel cortex, it was found that

a single microscopic lesion, similar in size, location and geometry to a human microinfarct, could produce tissue damage and perceptual deficits which could be mitigated with administration of memantine, a glutamate receptor antagonist (68).

Targeted Photothrombotic Occlusion

Targeted photothrombotic occlusion is a method by which ischemic damage is induced within a targeted cortical area by means of photo-activation of a previously injected light-sensitive dye. The dye Rose Bengal (4,5,6,7-tetrachloro-2',4',5',7'-tetraiodofluorescein) is one such photo-sensitizing agent. When Rose Bengal dye is illuminated with a 530nm laser, singlet oxygen is produced. In the intravascular environment, these free radicals damage components of endothelial cell membranes, leading to platelet aggregation and thrombi formation, eventually interrupting local blood flow (69). While diffuse light exposure has been used to generate large, non-specific strokes, emerging methods have been introduced to produce much smaller strokes, which mimic the nature of a CMI (70, 71). Using dichroic mirrors, a focused green laser may be introduced into the same optical pathways as the imaging laser used in a TPLSM system, allowing for photothrombosis to be targeted specifically to the lumen of an individual penetrating vessel (72). Following occlusion, the injury can be left to evolve into a lesion mimicking CMI.

Methods

Subjects

For this study, male mice from the C57BL/6 line were selected for use. Mice selected for the study were between 3 to 7 months of age at the time of the initial surgery, with an average age of 4.7 ± 1.2 months. The mean weight of the mice selected for the study was 27.2 ± 2.7 grams.

Study Design

Prior to the study, the timeline in **Figure 2** was developed to schedule surgery, habituation, and imaging. On day one, mice were implanted with a head-fixation flange imbedded in a skull cap. However, at this time a chronic window was not created in the skull to mitigate the deterioration of imaging quality later in the experiment.

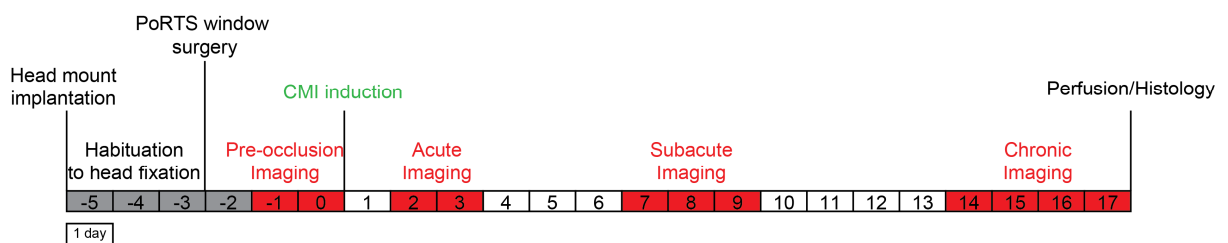


Figure 2. Timeline of experimental procedures

The initial surgical procedure was followed by four days of habituation to head fixation to prepare the mice for awake imaging sessions. On day four of

habituation, a PoRTS window was created over the left hemisphere of the mouse. The following day, pre-occlusion imaging was initialized, after which a single CMI was induced using photothrombosis in the barrel cortex. Post-occlusion imaging was then carried out in three time phases: acute (2-3 days post-occlusion), subacute (7-9 days), and chronic (14-17 days). Following the completion of chronic imaging, mice were sacrificed and perfused, and the tissue was labeled using immunohistochemistry techniques.

Surgical Procedure – Head Mount Implantation

Prior to the initiation of habituation, surgical procedures were performed to create a skull cap and implant a head-mount flange. Mice were first anesthetized with 4% isoflurane in air in an enclosed container. Once mice were in an anesthetized state as determined by the toe-pinch test, they were transferred to an apparatus under the surgical microscope with 1-2% isoflurane in air provided through a nose cone. At this time, mice were given a 50 μ l dose of .03mg/ml analgesic Buprenex (buprenorphine). The scalp of the mouse was sterilized with betadine followed by 30% ethanol. The toe-pinch test was performed again to ensure adequate depth of anesthesia before making any incision. Forceps were used to pinch and lift the scalp, which was removed with a single, clean incision using scissors. If any bleeding occurred at this point, sterilized kimwipes were employed to stop the flow of blood and to clean up the surgical site.

Sharp forceps were then used to remove the peri-osteum from the surface of the skull, exposing the bone. The skull surface was scored over the right hemisphere using the sharp forceps to allow for stronger binding with glue and dental cement. Additionally, the surface of the skull over the stereotaxic location of the vibrissa sensory cortex (3.5-4.0mm lateral from the midline and 1.2-2.0 mm caudal to bregma) was marked with a sterilized pencil. A wooden applicator was used to brush a thin layer of cyanoacrylate glue over the junction of the exposed skull and the edge of the incision, as well as over the top of pronounced sutures in the skull. This step is necessary to lock fluids away from the surface of the skull, which is critical when later creating the PoRTS window.

After allowing the cyanoacrylate glue to dry for 15 minutes, a custom titanium head mount flange was positioned over the right hemisphere of the skull, above the scored hash marks. Parkell C&B Metabond self-curing dental cement was applied to the exposed skull, with larger amounts about the head mount flange to anchor it to the skull. A thin layer was brushed over the demarcated vibrissa cortex, allowing the region to still be visually identifiable while protecting the skull from open exposure. The mice were then removed from the surgical apparatus and placed in their home cage under a heat lamp for recovery.

Habituation to Head Fixation

Following recovery from the initial surgery, the mice were gradually introduced to the long-term head fixation necessary for awake imaging in this

study. On each day, mice were placed into the imaging apparatus as detailed in **Figure 2**. Following brief isoflurane exposure, the mice were fixed to an anchored arm using the head mount flange and an adjustable cardboard tube was positioned snugly around the bodies of the mice to minimize movement. Mice that would later wear the pulse oximeter during imaging were conditioned with the MouseOx fixed to the left leg as well. On day one, habituation was carried out for 15 minutes, followed by 30 minutes on day two, 1 hour on day three, and 2 hours on day four. At the end of day four of habituation, mice that exhibited characteristics indicative of proper habituation were selected for PoRTS window surgery.

Surgical Procedure – PoRTS Window Surgery

Prior to the second surgical procedure, mice were anesthetized using the same techniques utilized before creating the skull cap and implanting the head-mount flange. Once mice were determined to be properly anesthetized using the tail pinch test, they were secured to the surgical apparatus using the head-mount flange. A dental drill was used at 10,000 rpm to delicately remove the dental cement over the demarcated vibrissa cortex. After removing the dental cement, exposing the underlying bone, the drill tip was replaced, as wear and tear resulting from drilling through the cement could be deleterious when drilling through bone. The skull was gradually thinned, periodically clearing debris using

an air canister and applying cool ACSF to the skull surface to dissipate heat created through the friction of drilling. The skull was determined to be adequately thinned when microvasculature became clearly visible with no aberrations following the application of ACSF, indicating a width of about 10-20 μm . The skull was then dried using kimwipes and the air canister. As shown in **Figure 3**, a thin layer of cyanoacrylate glue was applied to the thinned skull and a No. 0 coverslip was placed over the glue, resulting in a clear optical interface.

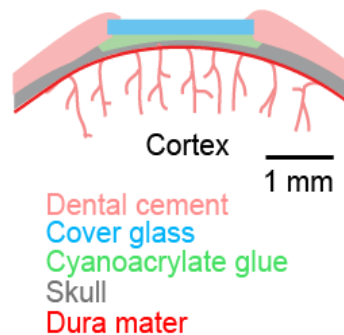


Figure 3. Schematic of PoRTS window for imaging mouse cortex.

Schematic showing the cross section of a PoRTS window. A thin layer of glue was applied to the thinned skull and a cover glass was placed above (73).

Imaging Setup

Imaging was performed using a custom Sutter two-photon microscopy setup powered by a tunable Coherent Ti-Sapphire laser. The freeware package MPScope 2.0 was used to control the laser scanning system (74, 75). Images and movies collected using this program were stored as .MPD files, a custom file

type, which allows for images across multiple channels to be packaged with co-synchronous signals if desired.

Mice were fixed into an imaging apparatus using the head mount flange and were additionally restrained with an adjustable cardboard tube. As shown below in **Figure 4**, an ADXL accelerometer was fixed to the cardboard tube to capture any strong incidences of movement, which may produce imaging artifacts during the study. An air puffer, supplied by a custom air-puffing system, was placed 2cm in front of the right vibrissa of the mice. An additional air puffer was angled at the base of the tail of the animal as a control for general sensory arousal.

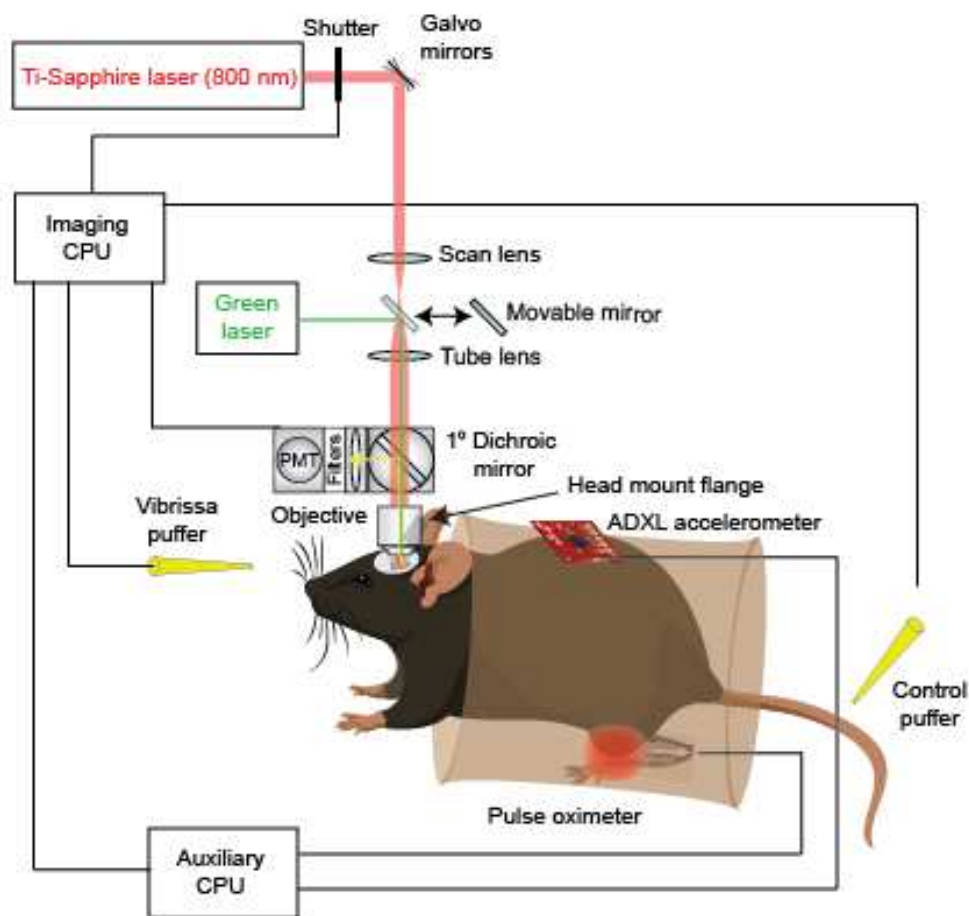


Figure 4. Schematic of Imaging Setup.

A tunable Ti-Sapphire laser provides excitation in the infrared range (800nm excitation was used for this study). Excitation light, which passes through the long-pass (700 nm cut-off) dichroic mirror, is focused, through the objective, to a very fine point which is rastered by scanning mirrors. Emission light passes back through the same objective, but is reflected by the dichroic mirror due to a higher wave frequency (shorter wavelength). Data was collected from the PMTs by an imaging computer, which was also used to drive the air-puff system. The imaging computer was linked to an auxiliary computer, which collected data from an ADXL accelerometer mounted on the restraint tube, for error correction, and physiological data from the pulse oximeter.

Imaging/Stimulation Procedure

At each time frame, imaging was performed in imaging sessions that did not exceed 4 hours over the course of one or more days. Prior to fixation in the imaging apparatus, mice were anesthetized in an enclosed container with 4% isoflurane until a deep plane of anesthesia was reached as determined by the toe pinch test. Once anesthetized, 0.05mL of 5.0% 2MDa FITC-dextran in PBS was introduced using a retro-orbital injection. If a noticeable deterioration in imaging quality attributable to declining dye concentrations was noticed during imaging sessions, the mouse was anesthetized with a nose-cone and re-injected with FITC.

Imaging of arteriole dilations was performed with a 20x Olympus objective with 1.0x digital zoom, a 512x400 pixel (312 x 244 μ m) imaging field, and a frame acquisition rate of 4.34 fps. For imaging with FITC-dextran, the excitation laser was tuned to 800nm and emissions were collected with a PMT with a filter passing green wavelengths.

Air puffers were supplied with 35 P.S.I. air and programmed to provide an 8 Hz duty cycle of 20ms open, 105ms closed, for 10 seconds. Areas of interest were determined by locating branching arterioles that exhibited a noticeable dilatory response to vibrissa stimulation. Four to six regions of interest were located per animal during pre-occlusion imaging.

To determine the dilatory properties of arterioles in each region of interest, a randomized stimulation paradigm consisting of 20 x 2-minute trials was performed. As shown in **Figure 5A**, each individual trial consisted of an initial baseline period of 30 seconds followed by 10 seconds of stimulation. After stimulation, a 50 second recovery period was included to allow arteriole conditions to recover to baseline. For each trial, the stimulation type was semi-randomized between vibrissa and tail stimulation so that 10 trials of each type occurred. Each individual trial was recorded as an individual .MPD file.

Following photothrombotic occlusion, the stimulation paradigm was carried out again in regions that were still imageable in the acute, subacute, and chronic time frames.

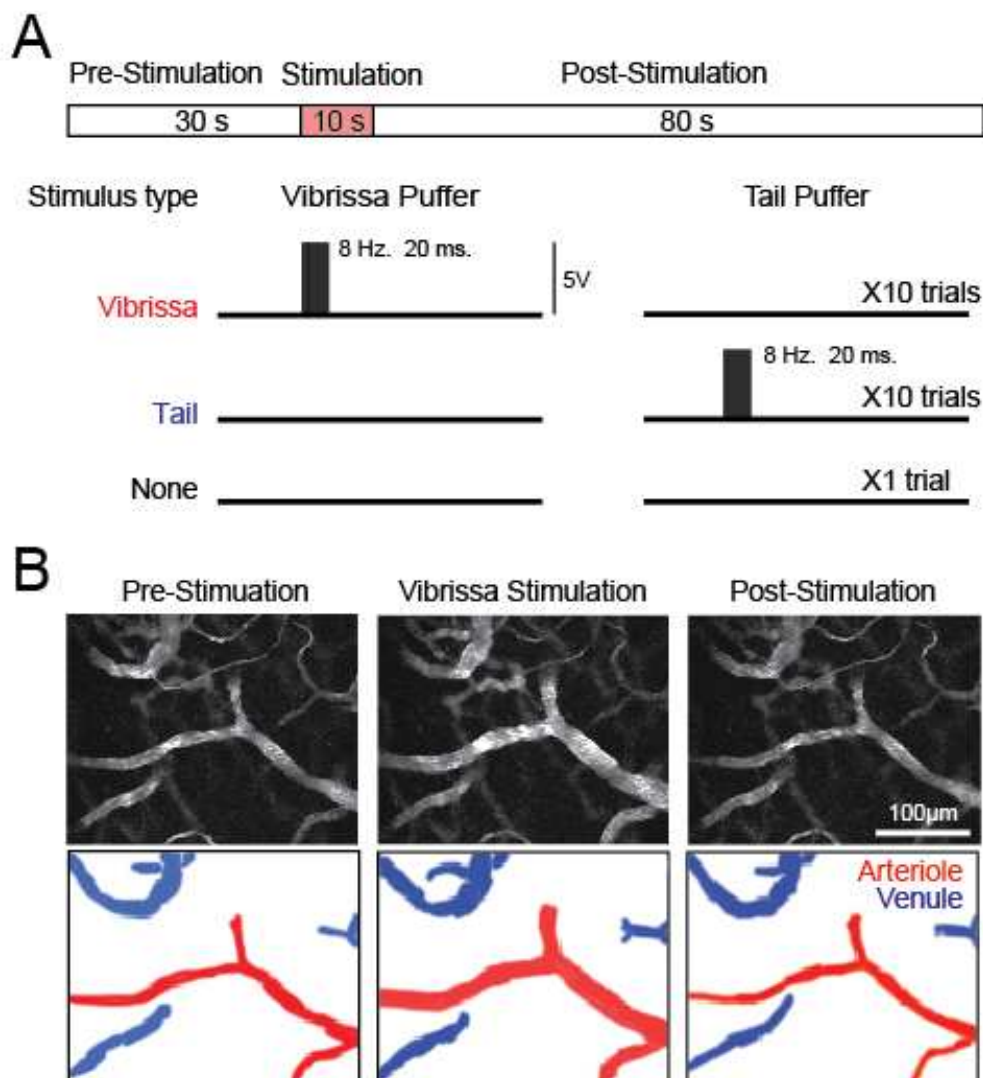


Figure 5. Stimulation Paradigm and Example of Dilation.

(A) Stimulation trials consisted of a 30 second pre-stimulation period, a 10 second stimulation period, and an 80 second post-stimulation period. 20 randomized trials, consisting of 10 vibrissa stimulations and 10 tail stimulations, were carried out to assess each region of interest. An additional 2 minute video was taken without stimulation to assess the quiescent behavior of the arterioles. (B) Example of arterioles dilating during vibrissa stimulation with traces showing arterioles and venules below.

Photothrombotic Stroke

Following the completion of pre-occlusion imaging, the mice were briefly anesthetized with 3% isoflurane in air supplied through a nosecone. Once a deep plane of anesthesia was reached, 0.025mL of 1.25% rose Bengal dye in PBS was injected retro-orbitally. Immediately after injection, isoflurane was discontinued. To aid in localization of the stroke to the barrel cortex, a penetrating arteriole previously observed to have a dilatory response to vibrissa stimulation was selected for targeted occlusion. After targeting the chosen arteriole with the two-photon system, a 530nm green laser was introduced along the microscope's light path with a moveable mirror, and focused through the objective to a point, 20 μ m in diameter, at the imaging plane, shown in **Figure 6**. The power of the green laser at its focus was 1 mW. The targeted penetrating arteriole was exposed to the laser for 30-45 seconds, during which the laser induced photolytic activation of circulating rose Bengal dye, creating free radicals, which in turn irritated the vascular wall initiating the clotting cascade.

After laser exposure, the two-photon system was used to image the targeted arteriole again to determine if occlusion was successful. If the arteriole failed to occlude, the vessel was targeted for green laser exposure again. Rose Bengal dye, which has a very short half-life, was re-injected, under anesthesia, if occlusion could not be achieved within 15 minutes. Mice were again briefly imaged at 30-minutes and 60-minutes to monitor for de-occlusion of the vessel.

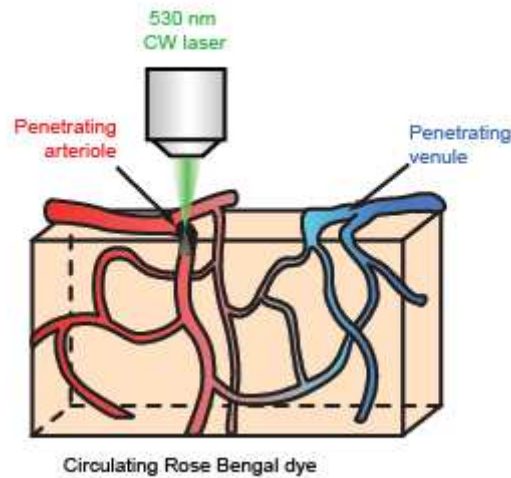


Figure 6. Schematic of Targeted Photothrombotic Occlusion of an Arteriole.

Intravenous Rose Bengal was activated with a green laser to produce ROS, causing vascular wall irritation and thrombosis.

Data Processing

Prior to analysis, output .MPD files were converted to a .tiff format for compatibility with matlab processing techniques. A custom matlab program was designed to handle bulk analysis of dilation data. As demonstrated in **Figure 7**, diameters of arterioles were determined by measuring the full-width half-maximum of the vessels. That is, the distance, when moving across the width of the vessel, from the first pixel that exceeds 50% of the intensity of the brightest pixel in the same cross-section, to the last such pixel.

Using a custom matlab program, the diameters of any number of arterioles within the imaging region could be measured by determining the average full-width half-maximum value for vessels within user-selected ROIs. As an output,

this analysis program gave a data structure containing individual diameter traces, such as those in **Figure 8**, for each vessel analyzed in each video.

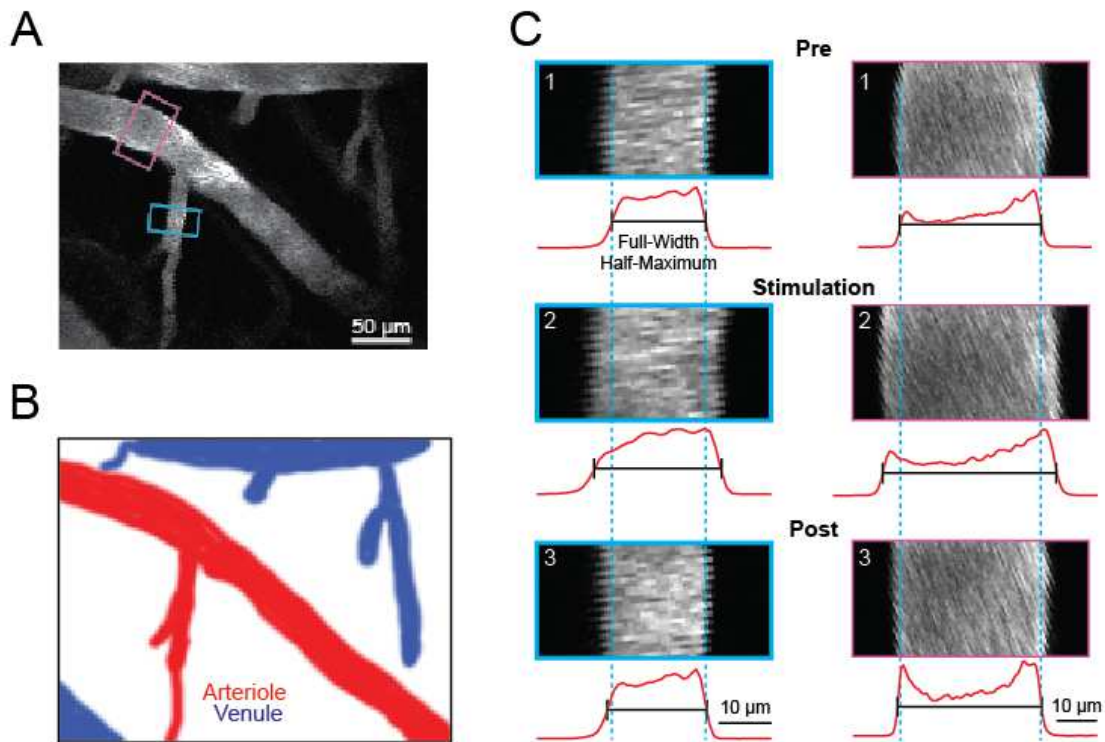


Figure 7. Example of Full-Width Half-Maximum Measurements of Dilating Arterioles

(A) Two-photon image of the pial network of surface vasculature, indicating two regions of interest (ROIs) positioned over surface arterioles. (B) Shading vessels in the image, with arterioles in red and venules in blue. (C) Full-width half-maximum (FWHM) measurements over before, during, and after vibrissa stimulation in the ROIs indicated in A. (D) Lumen diameter of the vessels within the ROIs over the course of a stimulation trial, as measured by FWHM.

A second custom program was utilized to compile data from these structures into average diameter traces for each vessel. After selecting a particular vessel from a region and a stimulus type (vibrissa or tail), the program incorporates Labchart output data from the ADXL accelerometer to screen out

data traces that contain movement artifacts which may cause aberrations. An average trace was then compiled from valid trials for the selected vessel.

Several parameters were calculated from these average diameter traces for analysis in this study. First, the average baseline diameter was calculated by taking the average diameter of the arteriole over at least 10 seconds during which spontaneous dilation does not occur during the 30 seconds preceding stimulation. The maximum dilation diameter and mean dilation diameter were taken as the maximum and mean diameter of the arteriole during the 10 seconds of stimulation. The maximum dilation percentage and the mean dilation percentage were calculated as the percent increase over the previously calculated baseline average for the two values.

To assess the temporal coupling of stimulus to response, the latency to dilation was calculated for each trace as the amount of time, in seconds, that elapses from the initiation of stimulation to the time point at which the arteriole diameter exceeds two standard deviations above the baseline average. Calculation of these parameters was automated and incorporated as a secondary function of the custom program.

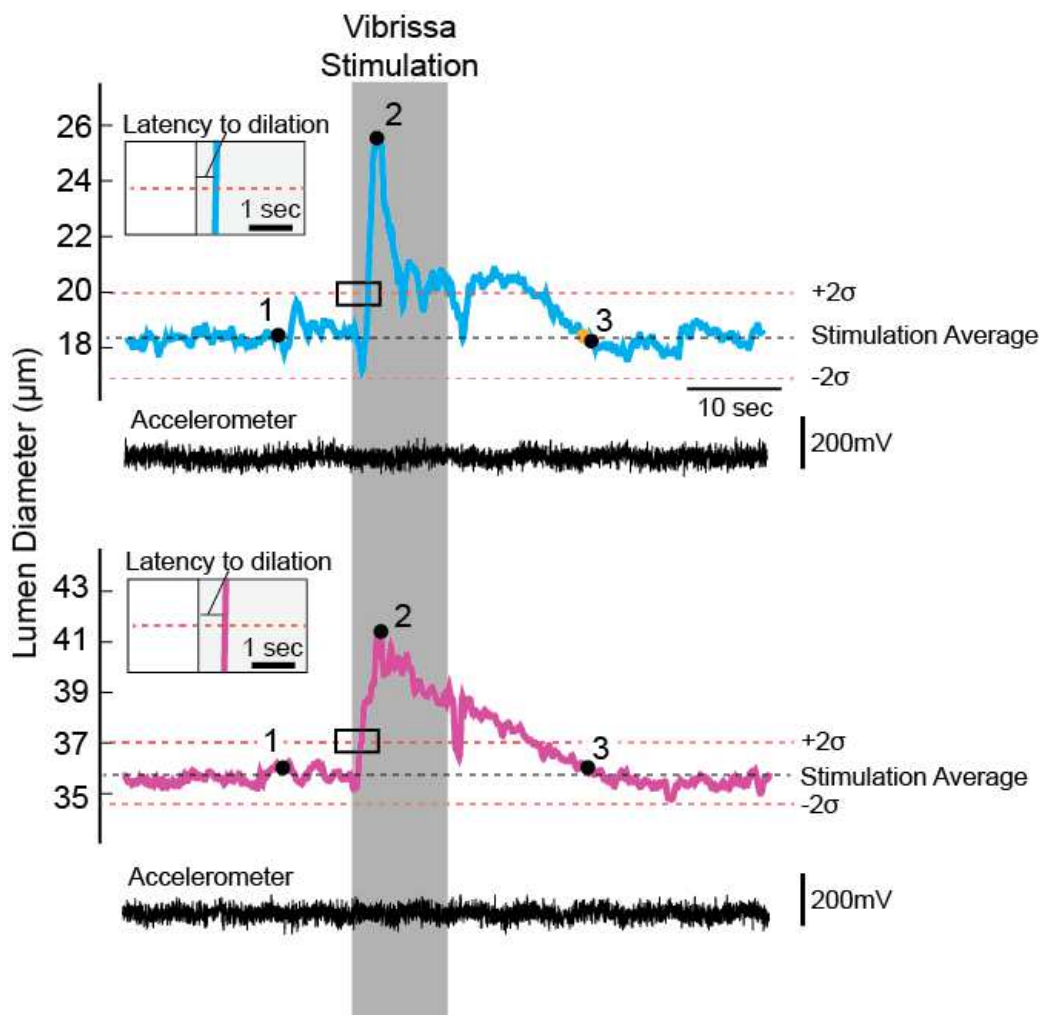


Figure 8. Vibrissa Stimulation Elicited Robust Dilation in Arterioles within the Vibrissa Cortex.

Dilatory traces from a single vibrissa stimulation trial in two arterioles. Accelerometers affixed to the restraint tube indicate no significant movement. Multiple trials are averaged using a custom program, and the latency to dilation, mean dilation, and max dilation are calculated from the average traces.

Immunohistochemistry

Following the completion of the chronic imaging session, the mice were injected with 0.1 mL of Euthazol and then trans-cardially perfused with 60mL PBS followed by 10mL 4% paraformaldehyde in PBS. The brain was then extracted and bisected into hemispheres. The cerebellum and striatum were delicately removed using forceps, and the remaining cortical hemispheres were flattened between two microscope slides separated by 1/16" and anchored together with two pairs of magnets placed at both ends of the slides. The microscope slide was then placed in a 60ml conical tube, submerging the brain tissue in 4% paraformaldehyde (15mL were added to each conical). The conical was then stored overnight at 4°C. After 24 hours, the 4% paraformaldehyde solution was replaced by PBS, and the conical tube was stored at 4°C until tissue was used for histology.

Prior to immunohistochemistry, flattened cortices of both hemispheres were removed from the microscope slides and sliced into 50µm sections using a vibratome. For primary antibody staining, tissue slices were placed in vials containing 2mL of antibody buffer (10 % (v/v) goat serum (Vector Labs), 2 % (v/v) Triton X-100, and 0.2 % (w/v) sodium azide) with 1:750 mouse anti-neun antibody (Millipore; MAB339), and 1:5,000 guinea pig anti-VGlu2 antibody (R&D Systems; AF1042) The tissue was incubated in the primary antibody solution for 24 hours on a nutating mixer. This was followed by a 30-minute wash in PBS. Next, the tissue was placed into a secondary solution consisting of antibody

buffer and 1:1,000 red anti-guineau pig (Invitrogen; A11076) and 1:1,000 blue anti-mouse (Invitrogen; A21049), and incubated for 2 hours. Next, another 30-minute wash in PBS preceded the placement of the tissue onto microscope slides which was then allowed to dry. Once dry, a coverslip was fixed to the slide using Fluoromount-G.

c-Fos Immunohistochemistry

The proto-oncogene c-Fos, which is robustly expressed in neurons following the firing of action potentials, was used as a tool to understand the extent of neural activity following induction of CMI. As it is upregulated from 60 to 90 minutes following neuronal activity, immunolabeling of c-Fos could reveal which neurons are responding to the vibrissa stimulation paradigm.

Immunohistochemistry was applied to label c-Fos in three mice for each time frame in this study. All mice were implanted with chronic thin-skull windows and habituated to fixation in the imaging apparatus as described previously. Vibrissa stimulation was utilized to locate dilating arterioles in the barrel cortex to target for occlusion. Three control mice were given sham occlusions, with focal green laser exposure but no Rose Bengal injection. Photothrombotic occlusion was induced in nine mice, three for each post-CMI time period. Prior to perfusion, mice were exposed to an 8hz train of 35 PSI air puffs to the contralateral vibrissa pad for 20 minutes. Mice were sacrificed and perfused as

previously described 75 minutes after stimulation. Mice with sham strokes were perfused on the day of the sham stroke, while the mice with CMIs were sacrificed at 48 hours (acute), 7 days (subacute), and 14 days (chronic).

Following perfusion, the brains were extracted and cortices of both hemispheres were flattened between microscope slides and submerged in 4% paraformaldehyde as previously detailed. For immunohistochemistry fluorescence labeling, tissue was first placed for 24 hours in a primary antibody labeling solution consisting of 1:500 rabbit anti-c-Fos (Santa Cruz Biotech; sc-52), 1:750 mouse anti-neun antibody (Millipore; MAB339), and 1:5,000 guinea pig anti-VGlu2 antibody (R&D Systems; AF1042) in antibody buffer. After a 30 minute wash, tissue was added to the secondary antibody labeling solution which consisted of 1:1,000 red anti-rabbit (Invitrogen; A11076), 1:1,000 green anti-gp (Invitrogen; A31268), and 1:1,000 blue anti-mouse (Invitrogen; A21049). For labeling c-Fos, the color red was selected over green due to the chance that residual FITC in the tissue could lead to inaccuracies when counting cells containing c-Fos.

This tissue was then mounted on slides using Fluoromount-G, and images were taken at 4x and 10x using a Leica fluorescence microscope. The locations of barrels within the barrel cortex were established using the VGlu2 staining and these parameters were taken into account when using a cell-counting macro in ImageJ, ITCN (Image-Based Tool for Counting Nuclei) to determine density of c-Fos activation in each barrel.

Results

Sensory-Evoked Arteriole Dilatory Response in Awake Mice

To assess the nature of evoked dilations in the healthy animal, data gathered during the pre-occlusion imaging phase was pooled together. A plot of the average dilatory response of arterioles and venules to the three stimulation conditions is shown below, in **Figure 9**. These traces were generated by compiling the average responses from all vessels imaged during the pre-occlusion period throughout the entire study. Vibrissa stimulation elicited a robust dilatory response, which was followed by an extended, steady-state dilation after the cessation of stimulation.

In contrast, tail stimulation as a control for general arousal resulted in brief arteriole dilation, which returned to baseline before the termination of stimulation. The specificity of vibrissa-evoked dilation suggested that arterioles sampled were within the barrel field of the primary sensory cortex. Although previous research has indicated venules exhibit a “bagpipe” capacitive effect following prolonged vibrissa stimulation, we found no evidence of venular dilation in this study under any stimulation conditions.

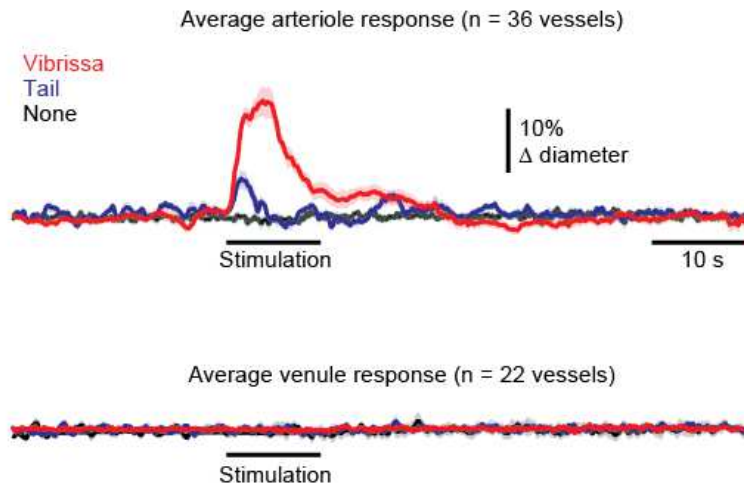


Figure 9. Average Responses of Arterioles and Venules to Stimulation under Basal Conditions.

Average diameter traces were calculated by averaging the traces for vibrissa stimulation, tail stimulation, and no stimulation from all arterioles and venules in pre-stroke conditions. Shading around the trace indicates standard error of the mean.

The average maximum dilatory response to vibrissa stimulation in arterioles resulted in a $23.6 \pm 5.9\%$ increase in diameter, while the average diameter during the course of stimulation was dilated $9.7 \pm 3.4\%$ over baseline values. In contrast, tail stimulation yielded an average maximum dilatory response of $4.1 \pm 1.3\mu\text{m}$ and an average mean dilation of $1.5 \pm 0.6\mu\text{m}$. As has been found in previous studies(76), there was a negative correlation ($r = -0.39$, $p < 0.01$) between baseline arteriole diameter and the degree to which arterioles dilate maximally.

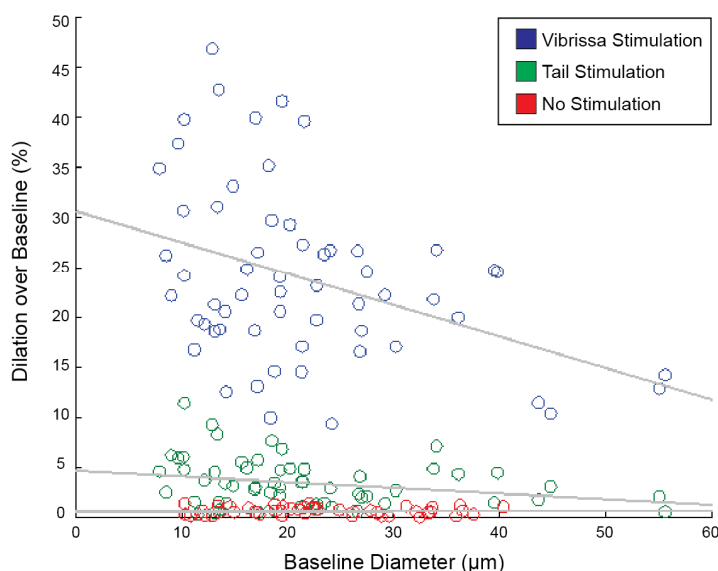


Figure 10. Maximum Dilatory Responses of Individual Arterioles to Stimulation under Basal Conditions.

There was no significant correlation between tail stimulation or no stimulation dilations and the baseline diameter. There was a significant negative correlation between the baseline diameter and the maximum dilation over baseline ($r = -0.4422$, $p = 0.01$)

Cerebral Microinfarcts were targeted to the Periphery of the Barrel Cortex

Following chronic imaging, mice were perfused and the brain tissue was labeled with IHC to determine the nature and location of CMIIs generated by the photothrombosis in this study, as shown in **Figure 11D**. The average radius of the generated strokes was $192 \pm 57.6 \mu\text{m}$. As indicated in **Figure 11E**, VGLUT2 labeling of the barrel cortex revealed that strokes were concentrated around the peripheral barrel cortex. The microinfarcts were strategically placed surrounding

the core barrels of the vibrissa field such that the gradient of their effect could be visualized over the imaging field.

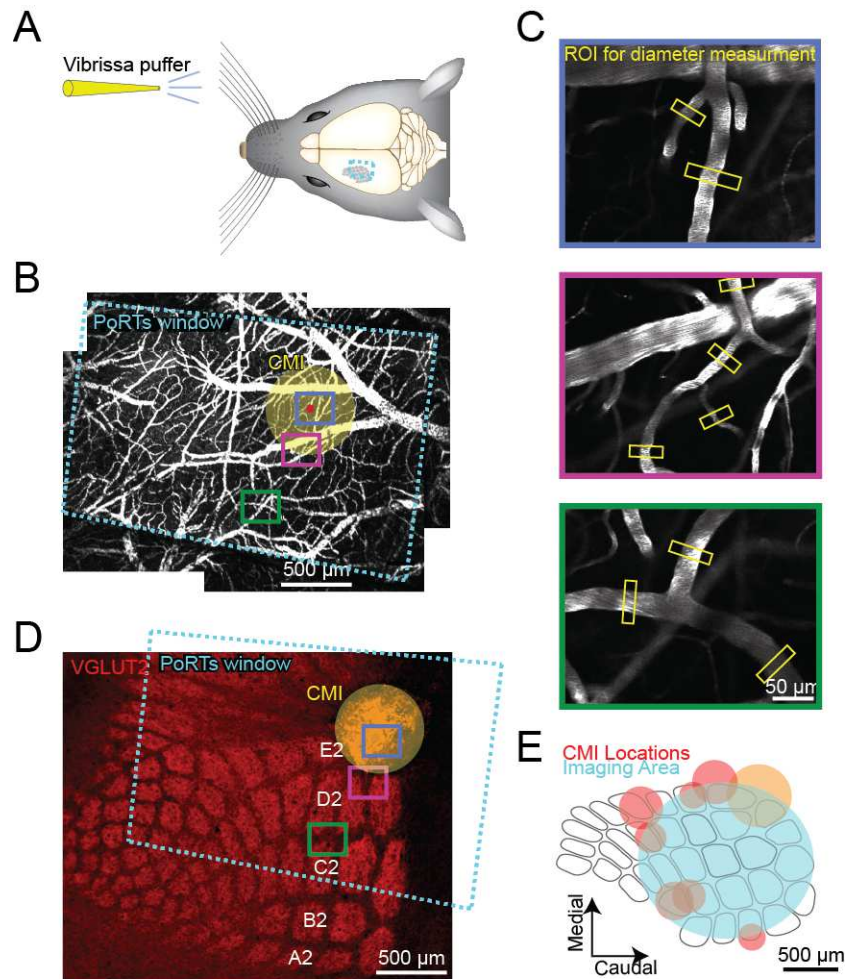


Figure 11. Locations of Imaging Regions and Cerebral Microinfarcts Within the Barrel Cortex

(A) The imaging window was situated over the left hemisphere vibrissa cortex, contralateral to stimulation. (B) 4x 2-Photon vasculature map showing the site of occlusion and three regions of interest. (C) 20x 2-Photon images of the regions of interest with yellow boxes indicating ROIs used for calculating vessel diameters. (D) VGLUT2 staining of the barrel cortex showing the location of a CMI. The location of the ROIs was transposed to this image using fiducials in the histology. (E) Location of CMIs within the barrel cortex, with the general imaging region indicated in blue. The CMI from D is indicated in orange.

Changes in Dilatory Response Following Cerebral Microinfarct

To assess changes in dilatory response following CMI, the stimulus responses from all viable vessels (those that could be located and identified in all time periods following occlusion) were averaged to provide a mean trace for the characteristic dilatory responses exhibited by arterioles over time.

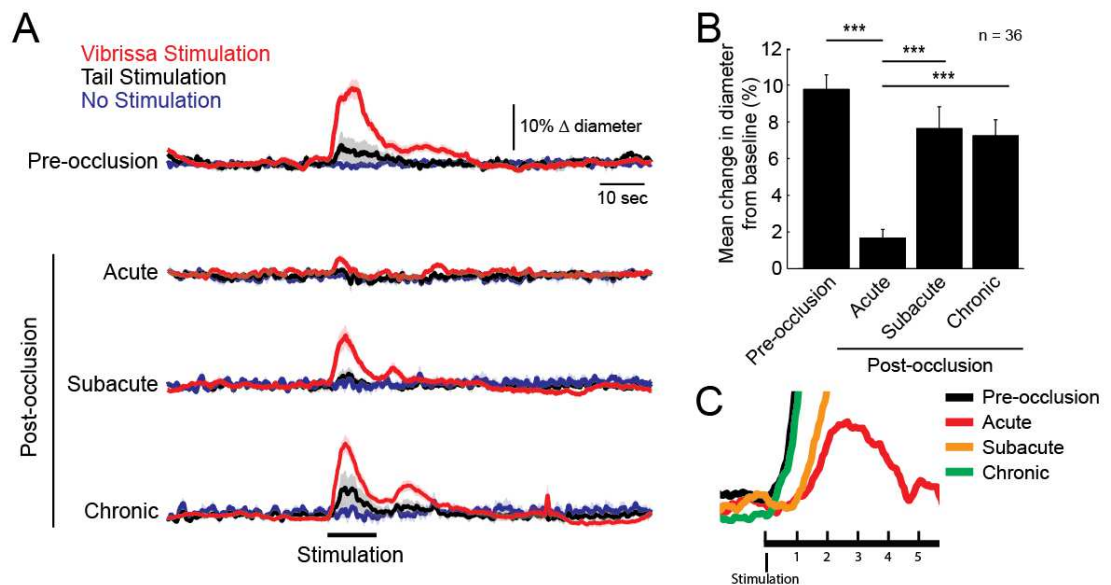


Figure 12. Average Dilatory Response of Arterioles Before and Following Occlusion.

(A) Average dilatory response of arterioles to the three stimulus condition presented. (B) Mean dilation over baseline was significantly attenuated in the acute phase, followed by significant recovery in the subacute and chronic phases. (C) Zoom-in of the first few seconds of stimulation reveals an increased latency to dilation in vessels during the acute and subacute time periods.

Following CMI, in the acute time phase there were obvious changes in the dilatory response to all forms of stimulation. Although there was still a small average dilatory response to vibrissa stimulation, the response is very brief and

greatly attenuated. Also, there is no evidence of a steady state response in the acute time phase. Further, tail stimulation produced no noticeable dilation.

When the same vessels were imaged again in the subacute time phase, a robust average dilation was restored in the vessels with a small steady-state response, albeit attenuated in magnitude compared to baseline. This was also evident in the chronic time-phase, when a small response to tail stimulation also returned. Taken together, this data suggests that there is a near-complete loss of dilatory response in the acute time phase, which partially recovers in the subacute time phase.

To give statistical power to the observations made concerning the average dilatory traces, the data from this study was compiled using a second method. The average trace across all viable trials for each vessel in each time frame was generated using the custom program. Baseline diameter, average dilation over baseline, maximum dilation over baseline, and latency to dilation were determined for each trace, and this data was compiled for each time frame for vessels from the same population of arterioles which could be visualized through all time frames. Shown in **Figure 13**, mean dilation over baseline during pre-stroke imaging was 9.8%, which significantly dropped to 1.8% in the acute time phase, followed by a recovery in the subacute and chronic phases during which the mean dilation was 7.6% and 7.1% respectively. Similarly, a significant loss of maximum dilatory capacity was also observed in the acute time phase, followed by significant recovery in the subacute and chronic time phases, as shown in

Figure 10. Additionally, there was a significant increase from pre-occlusion values in latency to dilation during the acute and subacute time periods. This was followed by a significant recovery of latency to dilation during the chronic time period.

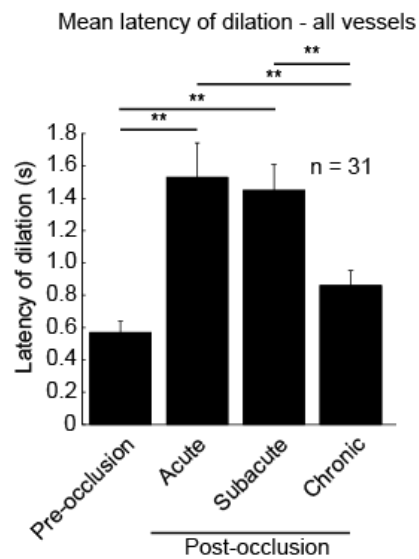


Figure 13. Mean Latency of Dilation is Augmented in the Acute and Subacute Time Periods.

Using a two-tailed t-test, the latency to dilation was compared between time periods. As indicated in the graph, pre-occlusion values were significantly lower ($p < 0.01$) than those in the acute and subacute time periods. Likewise, the mean latency in the chronic time period was significantly lower ($p < 0.01$) than in the acute and subacute time periods.

In previous studies, an inverse correlation has been noted between maximum dilation over baseline and the baseline diameter of an arteriole (76). When maximum dilation over baseline was plotted against the baseline diameter, the same correlation was found in the pre-CMI time period of this study; however, the correlation is completely abolished in acute time phase. There is partial

recovery of this trend later in the study, as the correlation re-emerged in the subacute and chronic time phases, albeit with a wider spread of responses.

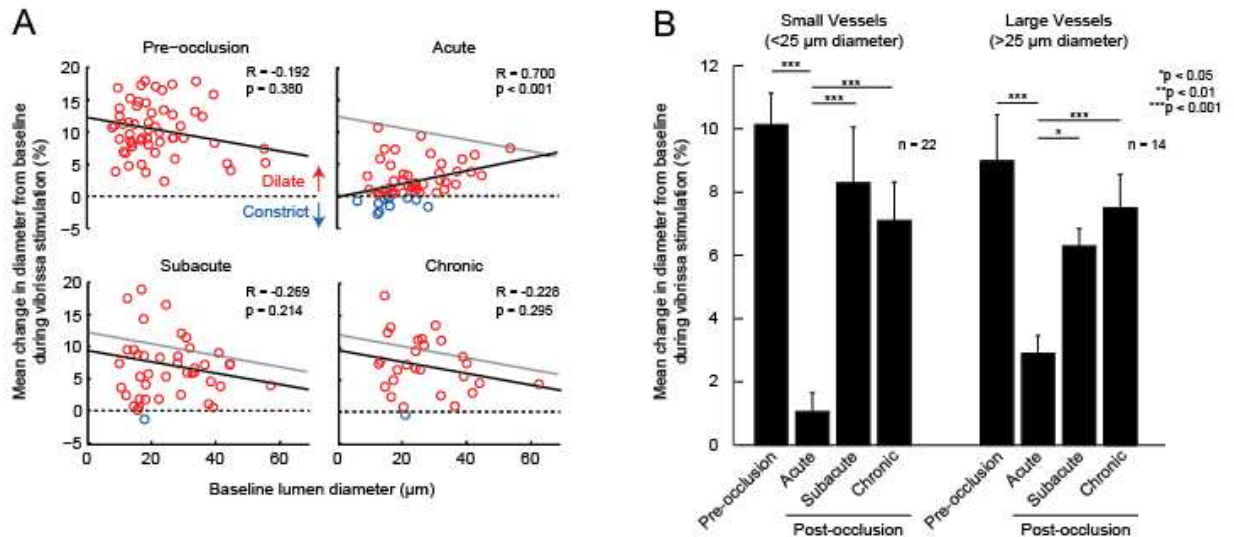


Figure 14. Loss of Dilatory Response in the Acute Time Phase effects both Small and Large Vessels.

(A) In the acute time phase, there was a positive correlation between baseline vessel diameter and the preserved dilatory response, however, the dilatory function of both small and large vessels was significantly attenuated in the acute time phase (B).

To determine whether the magnitude of the mean dilatory response might exhibit the same negative correlation to baseline diameter, the mean change in dilation from baseline was plotted against the baseline lumen diameter. In the pre-occlusion phase, there was a negative trend, but no significant correlation in contrast to what was observed with maximum dilation diameters, as shown in **Figure 14A**. Interestingly, a strong, positive correlation emerged in the acute phase, indicating that larger vessels may be capable of preserving greater

dilatory capacity. Although this trend was not preserved in the subacute and chronic phases, it points to the interesting conclusion that the effects of CMI may be more deleterious for neurovascular coupling in smaller vessels. In the acute phase there were a number of vessels that responded to vibrissa stimulation with a net negative dilation, potentially due to vascular steal.

To probe whether small vessels may have a different outcome than large vessels following CMI, the vessels were separated into two sub-populations, those less than and those greater than 25 μ m in baseline diameter. Indicated in **Figure 14B**, there was a significant loss in mean dilatory response in both sets of vessels during the acute time-phase followed by significant recovery in the subacute and chronic phases, indicating that the dilatory response for both sets of arterioles was similarly impacted following CMI.

Correlations between Changes in Dilatory Response and Position Relative to CMI

Dilatory responses were measured in vessels that covered a wide range of distances from the sites of targeted photothrombotic occlusions. As a strong loss of dilatory response was observed in the composite data from all vessels, varied locations of sampled vessels could elucidate whether this loss of dilatory response was a broad effect, or whether the bulk of changes in dilatory capacity took place in the immediate vicinity of the CMI. Shown in **Figure 15A**, the

dilatory responses for vessels, normalized to the pre-occlusion responses from the same vessels, were plotted against the distance from the putative stroke border as determined by 4x two-photon maps and VGlut2 IHC.

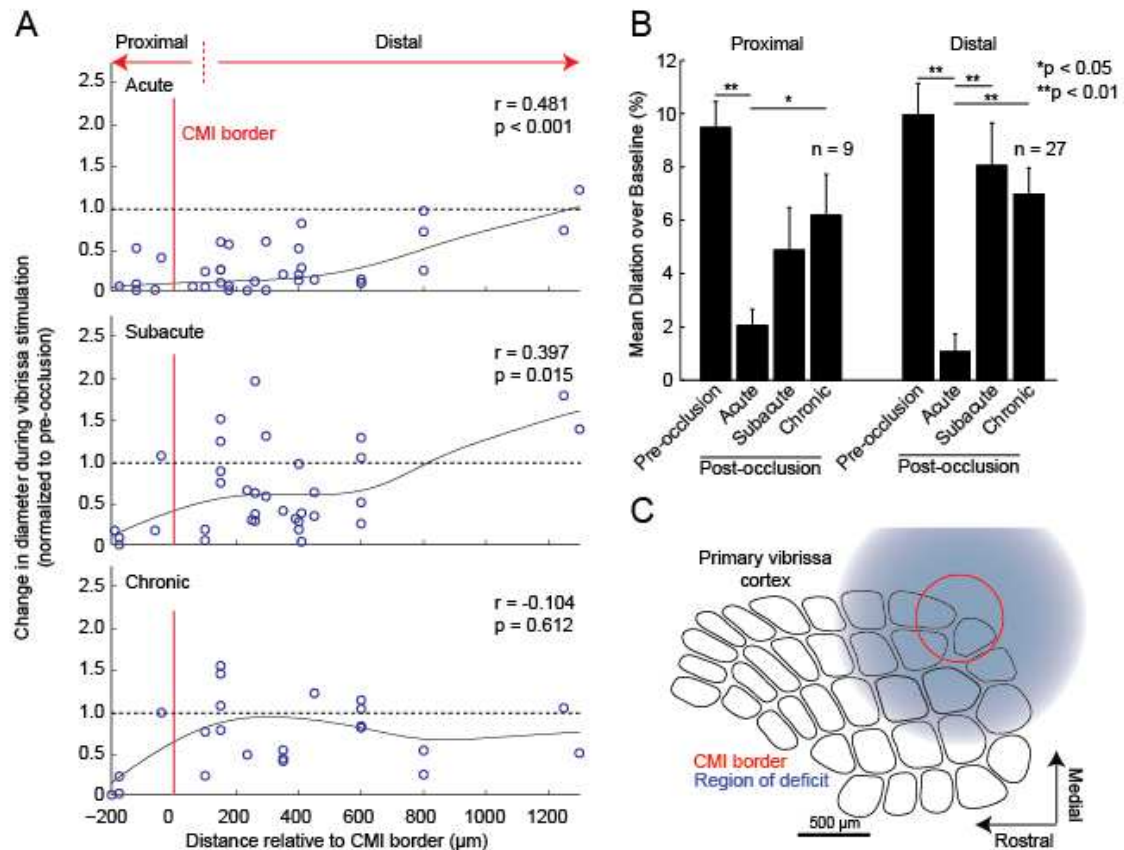


Figure 15. Loss of dilatory response extended far beyond the CMI border during the acute time phase.

(A) While vessels far outside of the CMI border were impacted in the acute time phase, there was a correlation between distance from the border and retained dilatory capacity. This trend was preserved through the subacute phase, indicating that distal vessels were impacted to a lesser extent and recovered quicker. (B) While both proximal and distal vessels saw significant decreases in dilatory capacity, there was significant recovery in distal vessels during the acute phase, while proximal vessels did not significantly recover until the chronic phase. (C) The region of deficit extended far beyond the stroke border in the acute time phase.

There was a significant positive correlation between the distance from the CMI border and the preserved dilatory capacity of arterioles during the acute and subacute time periods, indicating that vessels further from the border were more likely to preserve dilatory responses in those particular time frames.

To analyze whether distal and proximal vessels were differentially affected by CMI, the vessels analyzed in this study were broken into two groups, proximal, which were vessels within 100 μ m of the CMI border, and distal arterioles, located greater than 100 μ m away. The cut-off distance for this analysis was situated just outside of the overt CMI border, to account for a narrow ring of gliotic, non-normal tissue surrounding the CMI core. Arterioles within this cut-off included those in the immediate peri-infarct as well as the few viable arterioles within the CMI core. Both data sets saw a significant decrease in dilatory response; however, while distal arterioles exhibited a significant recovery beginning in the subacute time phase, proximal arterioles did not show significant recovery from acute dilatory responses until the chronic time phase. This indicates that both proximal and distal arterioles are similarly impacted by CMI in the acute time phase, but distal arterioles exhibit a quicker, more robust recovery in the subacute and chronic time phases. Nonetheless, this indicates that the loss of dilatory response extends far beyond the borders of the CMI during the early days following occlusion.

Change in latency, which was calculated as the change in time, in seconds, from latency to dilation for a given vessel during pre-occlusion imaging,

was also plotted against distance from the CMI border for all three post-stroke time phases in **Figure 16A**.

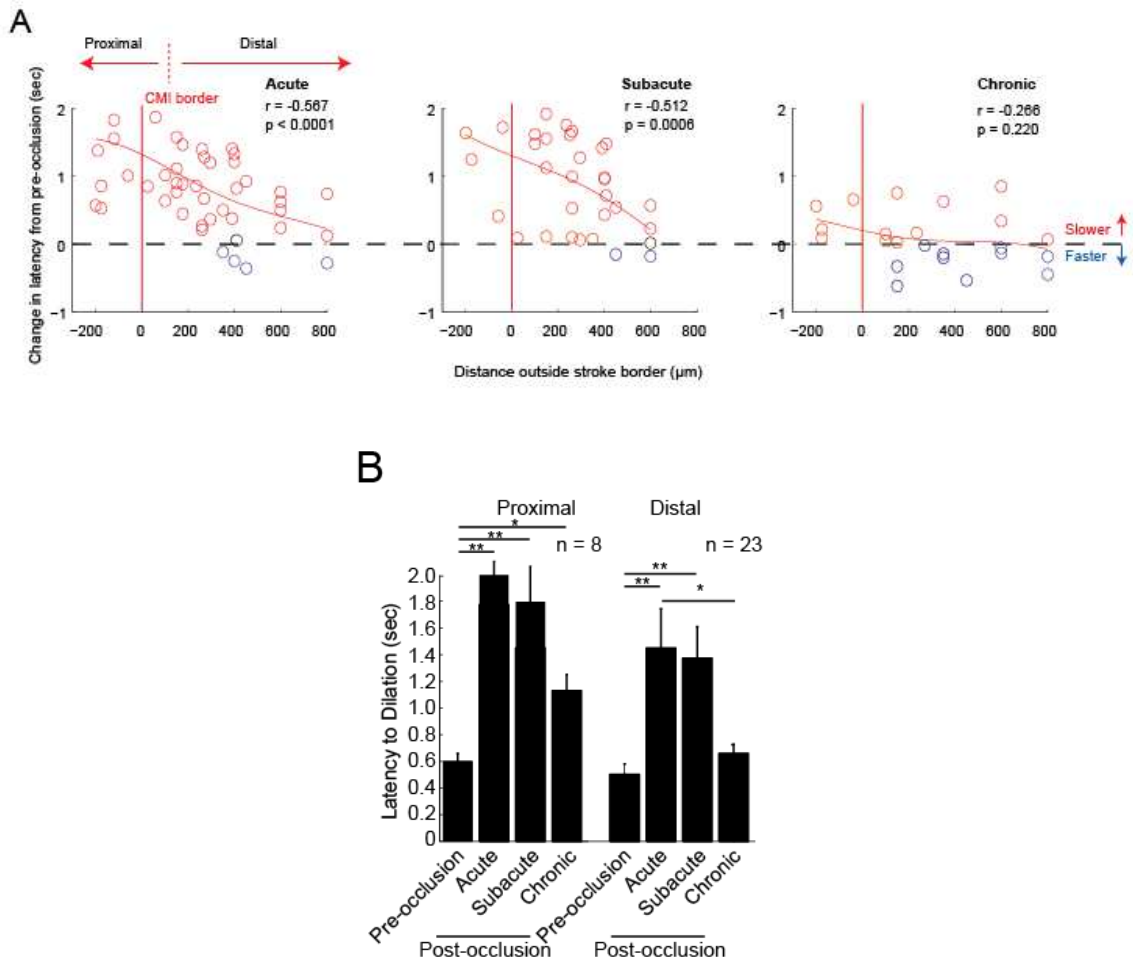


Figure 16. Both proximal and distal vessels experienced increase in latency to dilation following stroke.

(A) There was a negative correlation between distance from CMI border and increase in latency to dilation during the acute and subacute time periods, indicating that vessels proximal to the stroke were slower to dilate. (B) Both proximal and distal vessels exhibited increased latency to dilation in the acute and subacute time periods.

With this data, a strong negative correlation between distance from stroke border and change in latency was found in the acute and subacute time phases, indicating that vessels closer to the core of the CMI exhibited a greater latency to dilation. However, when latency data was broken into proximal and distal groups, both sets of data exhibited significant augmentation in latency to dilation in the acute and subacute time periods, followed by significant recovery in the chronic time period, indicating that CMIs are capable of broadly disrupting temporal neurovascular coupling.

Genesis of a Deficit – Neurovascular Coupling in Hyper-Acute Stage of Cerebral Microinfarction

To gain a better understanding of the means by which neurovascular deficits evolve from the initial occlusion to the broad effects measured at the acute phase, a separate, small cohort of mice were utilized to model the neurovascular hyper-acute (20 min. to 3 hrs. post-occlusion) time period following targeted photothrombotic occlusion of penetrating arterioles.

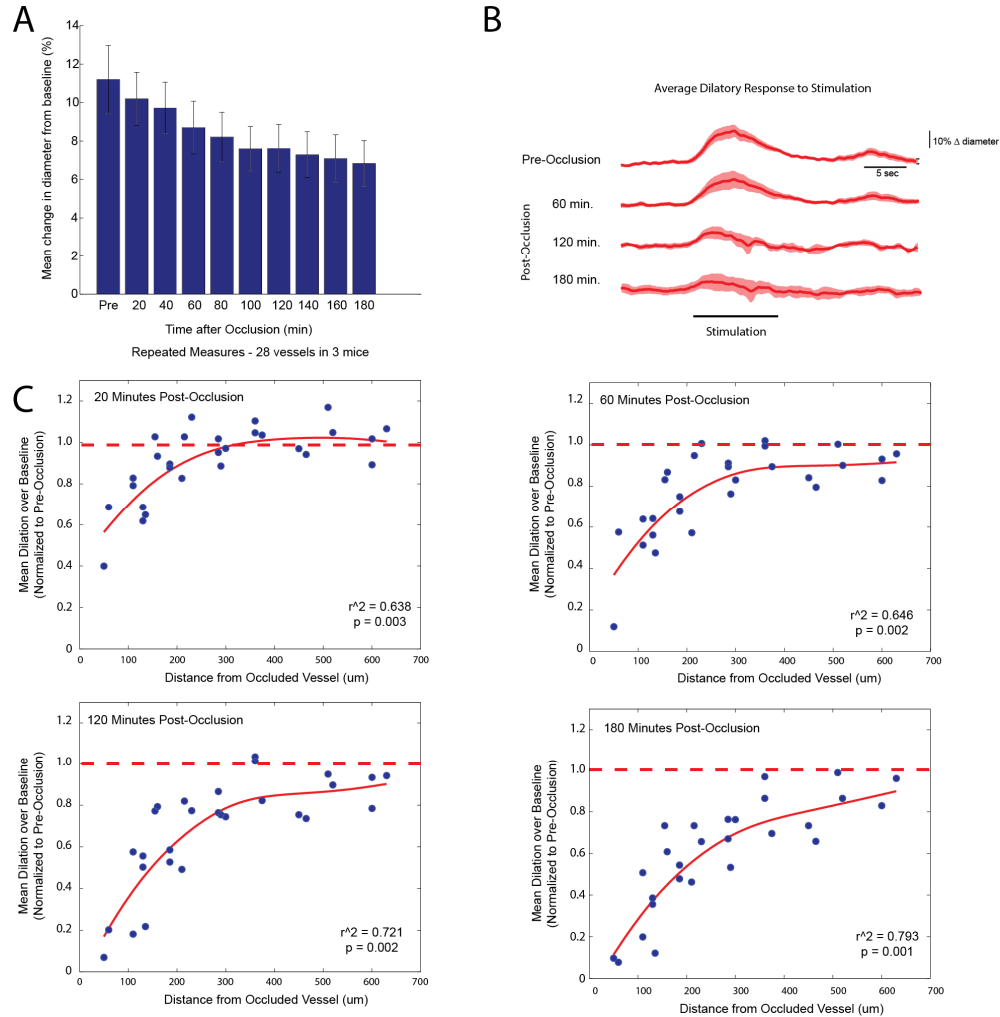


Figure 17: Neurovascular Coupling is Disrupted Proximal to Stroke in the Hyperacute phase.

A. Mean dilation over baseline rapidly diminished in repeatedly measured arterioles in the first three hours following microvascular occlusion. B. This loss of dilatory capacity is reflected in the average traces for arteriole dilation. C. Following targeted occlusion, there was a significant correlation between proximity to the occluded vessel and loss of dilatory function. This correlation became more pronounced over the course of hyperacute imaging.

As early as 20 minutes following the occlusion, dilatory deficits were found in many arterioles within 150 μ m of the occluded vessel. One hour following

occlusion, the dilatory deficit extends to 300 μ m from the occluded penetrating arteriole.

Isoflurane and c-Fos – Tools to Probe the Mechanisms of the Loss of Dilatory Response

The widespread loss of dilatory response found in the acute time phase indicates that there is at least a temporary breakdown of neurovascular coupling. This could be attributable to a number of factors, as there are a number of components that drive neurovascular coupling in the neurovascular unit. In this study, we chose to investigate the two candidates that are seemingly the most likely to be the source of this deficiency and the two principal components of the neurovascular unit, the sensory neurons which respond to stimuli, eventually driving vascular activity, and the vascular wall itself. To probe for deficits in neuronal activity, c-Fos, a proto-oncogene upregulated following extensive neuronal activity, was utilized to quantify neurons responding to the stimulus paradigm used in this study (77). Changes in vascular wall compliance were investigated using Isoflurane, a volatile anesthetic common in veterinary medicine, which is also a potent vasodilator (78).

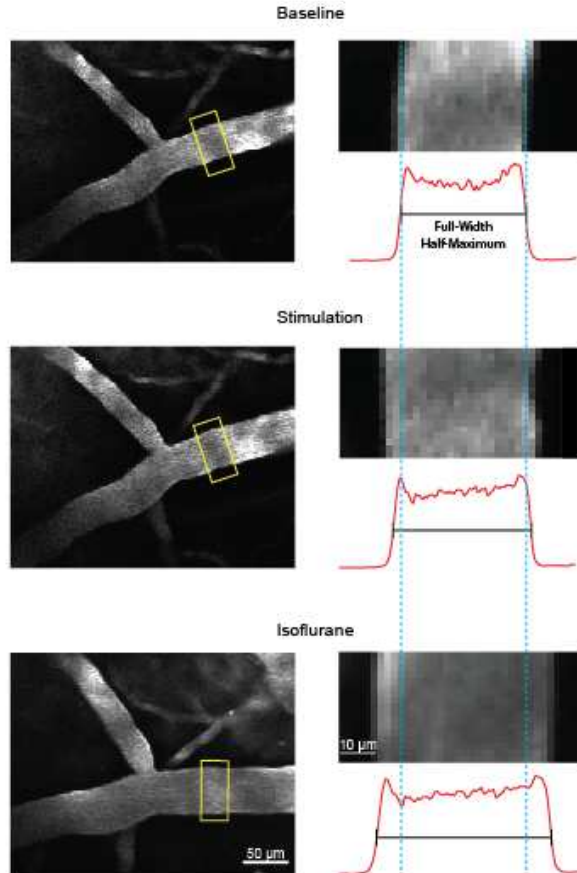


Figure 18. Isoflurane is capable of inducing far larger dilations than vibrissa stimulation.

Full-Width Half-Maximum measurements across the same arteriole reveal that isoflurane exposure induces dilations that exceed the dilatory response seen during vibrissa stimulation.

Isoflurane was administered to mice following imaging sessions at a concentration of 3.0% in air for 3 minutes. During this brief period of exposure, a movie was collected across all imaging regions to capture the extent of dilation during isoflurane exposure. The average dilation over baseline during isoflurane exposure was much greater than the maximum dilations achievable with the vibrissa stimulation paradigm during all time periods, indicating the vascular wall was capable of dilating well beyond the attenuated dilations seen following CMI.

Although this indicates that vascular wall stiffening cannot be the sole source of the loss of dilatory response, a significant decrease in isoflurane-induced dilations over baseline was evident in the acute phase, pointing toward vascular wall compliance issues as a potential contributing factor.

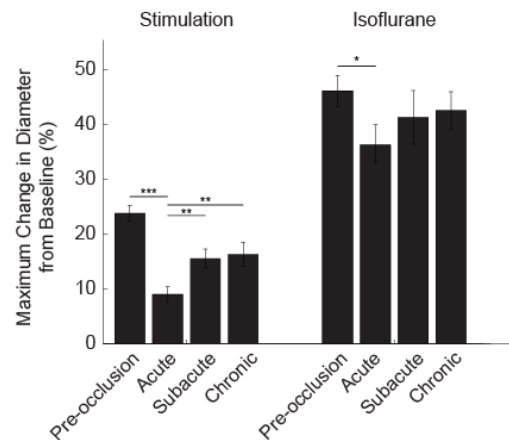


Figure 19. Dilations induced by isoflurane exposure were significantly attenuated in the acute phase, but still greatly exceeded the dilatory response to vibrissa stimulation.

Isoflurane was capable of dilating arterioles well beyond the maximum dilatory responses to stimulation during all time periods in this study. While there is a significant decrease in isoflurane induced dilation diameters in the acute time phase, these results indicate that it is unlikely that changes in vascular wall compliance are the only contributing factor to the loss of sensory-induced dilatory response seen in the acute phase.

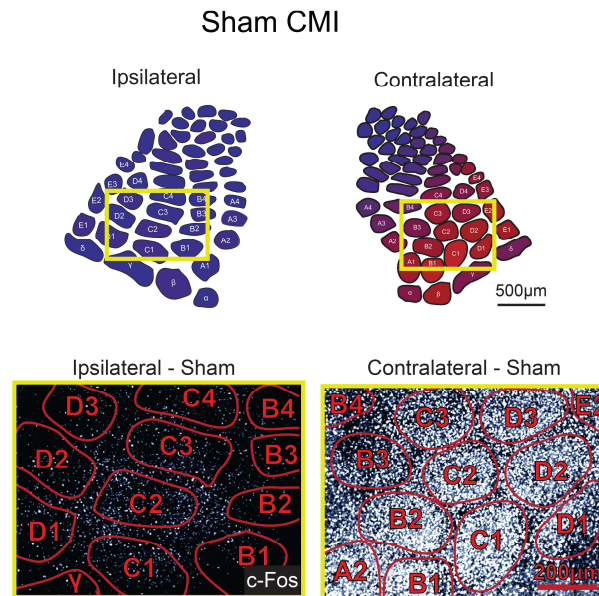


Figure 20. Immunofluorescence staining of c-Fos reveals robust neuronal activation in the barrel cortex contralateral to vibrissa stimulation in a sham animal.

In sham CMI animals, c-Fos was homogenously expressed at low levels throughout cortex ipsilateral to vibrissa stimulation, with a slight elevation in the primary vibrissa cortex. In the contralateral cortex, however, c-Fos was robustly expressed in the barrel cortex.

When mice were perfused during the acute time period following occlusion, the expression of c-Fos was reduced in a broad region of cortex extending up to 1mm outside of the stroke core, as shown in **Figures 21 & 22**.

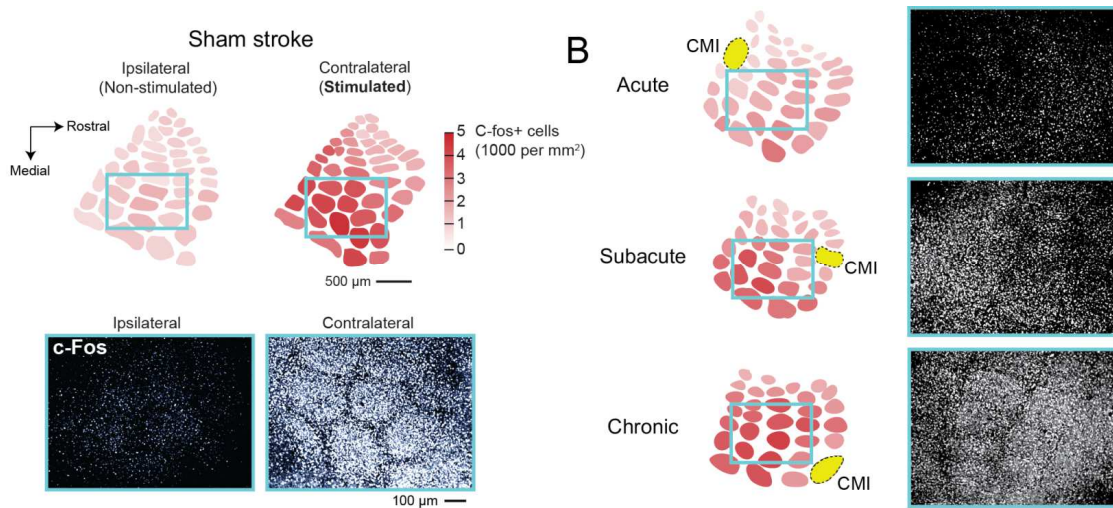


Figure 21. c-Fos activation in the barrel cortex contralateral to vibrissa stimulation is diminished in the acute phase following CMI.

Following CMI, the number of c-Fos+ cells in the barrel cortex is greatly reduced in the acute phase. As the CMI progresses into the subacute and chronic time periods, more cells were c-Fos+ in the peri-infarct cortex following prolonged vibrissa stimulation.

In mice that were sacrificed during the subacute time period, c-Fos levels began to recover from the acute deficit, with the region of inactive neurons extending only 200-400μm outside of the putative stroke border, shown in **Figure 22**. By the chronic time period, the expression of c-Fos had recovered even further, as many neurons within the peri-infarct strongly expressing the proto-oncogene following prolonged sensory stimulation. This data points toward a chronic, robust recovery of neurovascular coupling in the peri-infarct cortex.

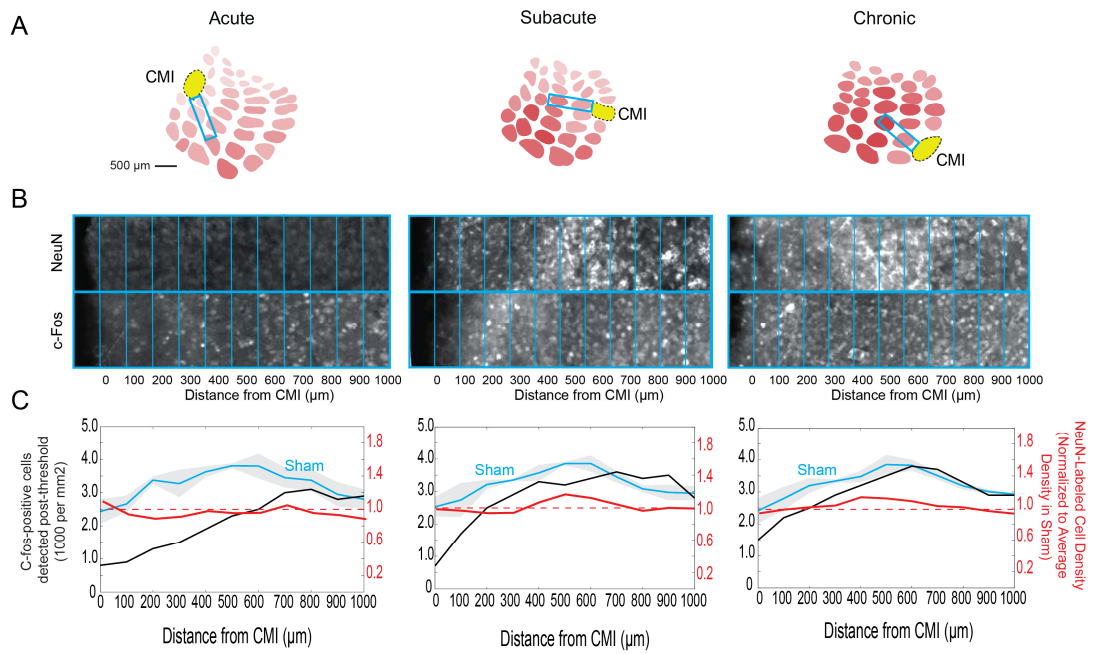


Figure 22. Expression of c-Fos is attenuated proximal to the CMI in the acute and subacute phases.

(A&B) A $100\mu\text{m} \times 500\mu\text{m}$ ROI was placed to sample c-fos activity as a function of distance from CMI. Another ROI was placed across the barrel cortex of a sham animal, covering the same barrels, to provide a control for basal stimulation expression. (C) c-Fos expression was reduced proximal to the CMI when compared to the control across the same barrel regions.

Discussion

The impact of microvascular lesions, as often observed in the aging human brain, on neurovascular coupling is currently not well understood. To probe this issue, we have utilized a mouse model of microinfarct pathology based on selective occlusion of individual penetrating arterioles and venules in the mouse barrel cortex. Neurovascular coupling was first assessed longitudinally by two-photon imaging of arterioles during vibrissa stimulation using air puffs during four time-periods: pre-occlusion, acute (2-3 days post occlusion), subacute (7-9 days post occlusion), and chronic (14-21 days post occlusion). The mean dilation from baseline diameter was significantly attenuated during the initial acute imaging period. Despite being relatively small in size ($\approx 400\mu\text{m}$ in diameter), CMLs generated in this experiment were capable of eliciting a widespread and persistent dilatory deficit in the surrounding cortex, with deficits occurring in arterioles up to 1mm outside of the putative stroke boundary.

The widespread impact of these targeted microvessel occlusions is likely attributable to the process of diaschisis, a term coined by van Monakow in 1914 to describe neurophysiological changes that occur distant to a focal brain lesion(79). These neurophysiological phenomena can be classified into two categories: Focal diaschisis, and connectional diaschisis. Focal diaschisis might occur during cortical strokes as the result of white matter tract degeneration in underlying subcortical tissue. While the microinfarcts induced in this study are unlikely to cause any form of extensive subcortical damage, it should be noted

that diffusion MRI studies in clinical stroke patients revealed that subcortical disconnection extends well beyond the locus of tissue necrosis, affecting major white matter pathways (80).

In the case of the targeted photothrombotic occlusions generated in this stroke model, it is more likely that expansive dilatory deficit is an example of connectional diaschisis, which encompasses changes in structural and functional connectivity between the lesion area and distal brain regions. While the barrel cortex is functionally segregated into barrels directly associated with individual vibrissa, there is still a high level of interconnectivity between barrels. Regular spiking pyramidal cells in layer 5 are tuned to respond to activity in surrounding barrels(81), while neurons in layer 2/3 also exhibit a high level of connectivity to surround barrels (82). Disruption of this inter-barrel connectivity could conceivably be contributing to the loss of neurovascular coupling in the days following CMI. A possible mechanism of this alteration in barrel-to-barrel connectivity may be remodeling the axon initial segment (AIS). AIS length is acutely decreased in the peri-infarct cortex, particularly affecting neurons with distal axons projecting in the infarcted area(42). The decrease in length occurs at the distal AIS, as axons essentially retract from the infarcted tissue, likely driving cortical reorganization. One limitation of the photothrombotic stroke model utilized is the potential for non-focal activation of intravenous rose-Bengal dye during targeted green laser illumination. Diffuse light below and adjacent to the site of occlusion could be causing low-level activation of rose Bengal dye,

generating free-radicals which could contribute to the ischemic damage observed well outside the infarcted tissue both in this study and in other studies utilizing photothrombotic stroke models. In addition to connectional diaschisis, widespread BBB breakdown observed in cortex during the subacute and chronic time periods both contralateral and ipsilateral to focal stroke may contribute to the broad effects of diaschisis(83, 84).

At the subacute imaging time frame, vessels exhibited significant, albeit incomplete, recovery from the dilatory deficit of the acute phase. Proximal vessels (those within 100 μ m of the putative stroke border) did not exhibit significant recovery of dilatory capacity during this time frame, indicating that deficit is likely prolonged in arterioles closer to the site of infarction, which is also suggested by a strong positive correlation between the distance from the stroke and the relative level of preserved dilatory capacity in the subacute phase. Previous research has provided evidence of broad hyperexcitability during the subacute phase in brain regions both ipsilateral and contralateral to ischemic stroke(85), which may drive the functional recovery of mean dilatory capacity in arterioles distal to the microinfarct. Electrophysiological paired-pulse studies in rat brain slices have shown extensive hyperexcitability in the contralateral hemisphere, as well as ipsilaterally as close as 1mm away from infarcted tissue.

Hyperexcitability has also been found seven days post occlusion with optogenetic mapping utilizing ChR2-evoked voltage sensitive dye responses(86). It should also be noted that, in the same study, regions distal to the infarct

exhibited upscaling of the evoked response, while connectomics analysis indicated that neurons closely connected to the peri-infarct were damaged whereas areas with little peri-infarct connection escaped damage, provide rationale to the often heterogeneous recovery observed in the tissue surrounding a stroke. While overt hyperexcitability was not detected in the form of an enhanced dilatory response, distal arterioles were more likely to preserve dilatory function in the acute phase, and exhibited significantly greater recovery in the subacute phase when compared to proximal arterioles. At the chronic time period, arterioles proximal to the CMI exhibited significant, yet incomplete, recovery of dilatory capacity from the acute deficit, which in effect abolished the correlation between dilatory function and proximity of arterioles to the infarct. This may indicate the recovery of neurovascular coupling in the spared cortex by way of functional reorganization and synaptogenesis.

The rapid, local deficit observed in the hyperacute experiment could be attributed to a number of mechanisms initiating in the early onset of stroke. In a model of focal ischemia, brain regions that exhibited severe ischemia (<10% of original CBF maintained) underwent rapid loss of spine and dendritic structure in as little as 10 minutes(87). The ensuing rapid spread of neurovascular decoupling is likely driven by secondary damage and proliferation of the stroke, initiated with the rapid release of ROS and pro-inflammatory mediators from apoptotic cells in the ischemic tissue(88). These mediators activate microglia, which are endogenously held in check by tonic inhibitory signaling,

morphologically altering the cells from a ramified to an amoeboid morphology and releasing inflammatory cytokines and chemokines which can exacerbate or conversely help repair ischemic injury(62). Specifically, the increased levels of cytokines and chemokines facilitate adhesion and trans-endothelial migration of circulation leukocytes(89). These infiltrating leukocytes may release pro-inflammatory mediators, including cytokines, chemokines, and ROS which contribute to the evolution of tissue damage(90) and drive the infiltration of various inflammatory cells, including neutrophils, t-cell subtypes, and additional monocytes and macrophages(91). In addition to the biochemical impact of rolling leukocytes within the microvasculature, leukocyte adhesion might mechanically limit vascular perfusion of the infarcted tissue, as frequent flow stagnation of deep cortical capillaries has been observed due to leukocyte plugging in a mouse model of hypoperfusion(92).

In addition to the deficits seen in dilatory capacity, targeted CMIs also appeared to impact neurovascular coupling by significantly prolonging the latency to dilation during vibrissa stimulation in both the acute and subacute time periods. There was also a significant correlation between the proximity of arterioles to the CMI and the increase in latency to dilation, indicating that, in addition to causing broad dilatory deficits, CMIs have a stronger deleterious effect on temporal neurovascular coupling in arterioles proximal to the infarct. This adjustment in temporal neurovascular coupling may reflect the ongoing process of axonal rewiring during recovery from ischemic stroke, which is

facilitated by inhibition of growth inhibitory molecules in the peri-infarct for up to 1 month following injury. Axonal rewiring occurs in three phases following stroke(93). In the early phase, from days 1 to 3, rhythmic and synchronized neuronal discharges, similar to those in the developing brain, induce axonal sprouting. Starting at day 3, genes for growth cone lipid raft proteins GAP43, Cap23, and MARCKS as well as the transcription factor c-Jun are induced and persist through the duration of the sprouting process(94). The increased latency to sensory induced dilation present in the acute phase, and persisting to the subacute phase, could be attributed to shifting functional connectivity. Axons projecting into the region of infarction are pruned, while immature spines forming on surviving neurons in the peri-infarct have yet to establish strong functional connections, leaving a relatively disjointed system that is slow to respond to stimulus. In the middle phase of the sprouting response, cell adhesion molecules help guide the sprouting response and form new connections. The final stage of the sprouting process involves cytoskeletal reorganization genes SCG10 and SCLIP, which aide in the maturation of the sprouting process. This final maintenance phase initiates 7-14 days post ischemia, and results in the formation of an anatomically distinct pattern of connections(93).

To further investigate our findings, we utilized two assessments to ascertain whether the source of the deficits might be attributable to alteration in vascular mechanics, or in neuronal signaling. Vascular alterations occurring in the early stages following stroke include the adoption of tortuous morphologies in

penetrating vessels(95), leukocyte rolling and adhesion(92), and swollen and vacuolated endothelial cells(83), all of which can impact CBF. Acute isoflurane administration was performed before occlusion, and in the acute, subacute, and chronic phase to investigate whether endothelial cell alterations might mechanically inhibit vascular dilation. Isoflurane induced dilations were significantly attenuated in the acute time phase, coinciding with the most significant dilatory deficits, however, there was recovery to baseline in the subacute and chronic phases. Isoflurane induces vasodilation of cerebral vessels at least partially through the activation of ATP-sensitive K⁺ channels on the endothelial cells(78), a pathway also present in the neurovascular signaling unit(15). A reduction of these receptors, or a deficit in endothelial cell reactivity to them, may contribute to the dilatory deficit observed in the peri-infarct following cerebral microinfarction. In addition, it has been found that vascular smooth muscle F-actin is reduced following 1 hour of middle cerebral artery occlusion, which could be promoting vascular damage and limiting vascular wall compliance(96).

Due to the complexity of neurovascular coupling, we used the proto-oncogene c-Fos, which is upregulated following strong neuronal activation, as a simple probe to determine whether viable neurons in the peri-infarct were capable of responding to sensory stimuli. c-Fos expression was greatly reduced in the acute mouse, with severe deficits extending up to 1mm from the ischemic stroke core. While previous studies have indicated that endogenous c-Fos is

briefly upregulated following focal ischemia(97, 98), with peak values occurring at 60 minutes post occlusion, the time point used for this study does not coincide with these findings, and no upregulation of c-Fos activity is indicated in our results. Instead, widespread deficits that present acutely persist into the subacute time phase, indicating poor neuronal connectivity during a period of synaptogenesis and neuronal rewiring.

The results of this study help to shed light on the microvascular environment and on alterations in neurovascular coupling at the level of individual vessels, and provide a microvascular correlate to previous BOLD fMRI findings. The data in this study reveals that CMLs, though small in size, can impact neurovascular coupling in a broad region of cortex, elucidating a mechanism by which microinfarcts may cause cognitive impairment. As CMLs have previously been associated with dementia in the elderly, these findings indicate that the neurovascular unit, in addition to being a crucial component in stroke therapy, may be a crucial target for therapeutic approaches to dementia in the future.

References

1. Attwell D, Laughlin SB. An energy budget for signaling in the grey matter of the brain. *Journal of Cerebral Blood Flow & Metabolism*. 2001;21:1133-45.
2. Mchedlishvili G. *Arterial Behavior and Blood Circulation in the Brain*. New York: Consultants Bureau; 1963.
3. Blinder P, Shih AY, Rafie CA, Kleinfeld D. Topological basis for the robust distribution of blood to rodent neocortex. *Proceedings of the National Academy of Sciences USA*. 2010;107:12670-5.
4. Schaffer CB, Friedman B, Nishimura N, Schroeder LF, Tsai PS, Ebner FF, Lyden PD, Kleinfeld D. Two-photon imaging of cortical surface microvessels reveals a robust redistribution in blood flow after vascular occlusion. *Public Library of Science Biology*. 2006;4:258-70.
5. Devor A, Tian P, Nishimura N, Teng IC, Hillman EM, Narayanan SN, Ulbert I, Boas DA, Kleinfeld D, Dale AM. Suppressed neuronal activity and concurrent arteriolar vasoconstriction may explain negative blood oxygenation level-dependent signaling. *Journal of Neuroscience*. 2007;27:4452-9.
6. Derdikman D, Hildesheim R, Ahissar E, Arieli A, Grinvald A. Imaging spatiotemporal dynamics of surround inhibition in the barrels somatosensory cortex. *Journal of Neuroscience*. 2003;23:3100-5.
7. Blinder* P, Tsai* PS, Kaufhold JP, Knutsen PM, Suhl H, Kleinfeld D. The murine cortical angiome: An interconnected vascular network with noncolumnar patterns of blood flow. *Nature Neuroscience*. 2013;16:889-97.
8. Shih AY, Driscoll JD, Drew PJ, Nishimura N, Schaffer CB, Kleinfeld D. Two-photon microscopy as a tool to study blood flow and neurovascular coupling in the rodent brain. *Journal of Cerebral Blood Flow & Metabolism*. 2012;32(7):1277-309.
9. Purves D, Augustine GJ, Fitzpatrick D, et al., editors. *Neuroscience*. 2nd edition. Sunderland (MA): Sinauer Associates; 2001. *The Blood Supply of the Brain and Spinal Cord*. Available from: <http://www.ncbi.nlm.nih.gov/books/NBK11042/>
10. Berg JM, Tymoczko JL, Stryer L. *Biochemistry*. 5th edition. New York: W H Freeman; 2002. Section 30.2, Each Organ Has a Unique Metabolic Profile. Available from: <http://www.ncbi.nlm.nih.gov/books/NBK22436/>

11. Jones M, Hewson-Stoate N, Martindale J, Redgrave P, Mayhew J. Nonlinear coupling of neural activity and CBF in rodent barrel cortex. *Neuroimage*. 2004;22(2):956-65. doi: 10.1016/j.neuroimage.2004.02.007. PubMed PMID: 15193627.
12. Buxton RB, Uludag K, Dubowitz DJ, Liu TT. Modeling the hemodynamic response to brain activation. *Neuroimage*. 2004;23:S220-33.
13. Lee SP, Duong TQ, Yang G, Iadecola C, Kim SG. Relative changes of cerebral arterial and venous blood volumes during increased cerebral blood flow: Implications for BOLD fMRI. *Magnetic Resonance in Medicine*. 2001;45:791-800.
14. Ogawa S, Lee TM, Kay AR, Tank DW. Brain magnetic resonance imaging with contrast dependent on blood oxygenation. *Proceedings of the National Academy of Sciences USA*. 1990;87:9868-72.
15. Hawkins BT, Davis TP. The blood-brain barrier/neurovascular unit in health and disease. *Pharmacological reviews*. 2005;57(2):173-85. doi: 10.1124/pr.57.2.4. PubMed PMID: 15914466.
16. Abbott NJ, Rönnbäck L, Hansson E. Astrocyte-endothelial interactions at the blood-brain barrier. *Nature Reviews of Neuroscience*. 2006;7:41-53.
17. Denk W, Strickler JH, Webb WW. Two-photon laser scanning fluorescence microscopy. *Science*. 1990;248(4951):73-6. PubMed PMID: 2321027.
18. Helmchen F, Denk W. Deep tissue two-photon microscopy. *Nature Methods*. 2005;2:932-40.
19. Sims NR, Muyderman H. Mitochondria, oxidative metabolism and cell death in stroke. *Biochim Biophys Acta*. 2010;1802(1):80-91. doi: 10.1016/j.bbadis.2009.09.003. PubMed PMID: 19751827.
20. Roger VL, Go AS, Lloyd-Jones DM, Benjamin EJ, Berry JD, Borden WB, Bravata DM, Dai S, Ford ES, Fox CS, Fullerton HJ, Gillespie C, Hailpern SM, Heit JA, Howard VJ, Kissela BM, Kittner SJ, Lackland DT, Lichtman JH, Lisabeth LD, Makuc DM, Marcus GM, Marelli A, Matchar DB, Moy CS, Mozaffarian D, Mussolino ME, Nichol G, Paynter NP, Soliman EZ, Sorlie PD, Sotoodehnia N, Turan TN, Virani SS, Wong ND, Woo D, Turner MB. Heart disease and stroke statistics--2012 update: a report from the American Heart Association. *Circulation*. 2012;125(1):e2-e220. Epub 2011/12/20. doi: CIR.0b013e31823ac046 [pii]
21. Murphy SL, Xu J, Kochanek KD. Deaths: final data for 2010. *National vital statistics reports : from the Centers for Disease Control and Prevention, National*

Center for Health Statistics, National Vital Statistics System. 2013;61(4):1-117. PubMed PMID: 24979972.

22. Go AS, Mozaffarian D, Roger VL, Benjamin EJ, Berry JD, Blaha MJ, Dai S, Ford ES, Fox CS, Franco S, Fullerton HJ, Gillespie C, Hailpern SM, Heit JA, Howard VJ, Huffman MD, Judd SE, Kissela BM, Kittner SJ, Lackland DT, Lichtman JH, Lisabeth LD, Mackey RH, Magid DJ, Marcus GM, Marelli A, Matchar DB, McGuire DK, Mohler ER, Moy CS, Mussolino ME, Neumar RW, Nichol G, Pandey DK, Paynter NP, Reeves MJ, Sorlie PD, Stein J, Towfighi A, Turan TN, Virani SS, Wong ND, Woo D, Turner MB. Heart disease and stroke statistics--2014 update: a report from the American Heart Association. *Circulation*. 2014;129(3):e28-e292.

23. Dirnagl U, Iadecola C, Moskowitz MA. Pathobiology of ischaemic stroke: An integrated view. *Trends in Neurosciences*. 1999;22(9):391-7. doi: 10.1016/S0166-2236(99)01401-0.

24. Schubert D, Piasecki D. Oxidative glutamate toxicity can be a component of the excitotoxicity cascade. *The Journal of neuroscience : the official journal of the Society for Neuroscience*. 2001;21(19):7455-62. PubMed PMID: 11567035.

25. Benveniste H, Drejer J, Schousboe A, Diemer NH. Elevation of the extracellular concentrations of glutamate and aspartate in rat hippocampus during transient cerebral ischemia monitored by intracerebral microdialysis. *J Neurochem*. 1984;43(5):1369-74. PubMed PMID: 6149259.

26. Novelli A, Reilly JA, Lysko PG, Henneberry RC. Glutamate becomes neurotoxic via the N-methyl-D-aspartate receptor when intracellular energy levels are reduced. *Brain research*. 1988;451(1-2):205-12. PubMed PMID: 2472189.

27. Olney JW, Price MT, Samson L, Labruyere J. The role of specific ions in glutamate neurotoxicity. *Neuroscience letters*. 1986;65(1):65-71. PubMed PMID: 2871531.

28. Rothman SM, Olney JW. Glutamate and the pathophysiology of hypoxic--ischemic brain damage. *Annals of neurology*. 1986;19(2):105-11. doi: 10.1002/ana.410190202. PubMed PMID: 2421636.

29. Benveniste H, Jorgensen MB, Diemer NH, Hansen AJ. Calcium accumulation by glutamate receptor activation is involved in hippocampal cell damage after ischemia. *Acta neurologica Scandinavica*. 1988;78(6):529-36. PubMed PMID: 2906199.

30. Brennan KC, Romero Reyes M, López Valdés HE, Arnold AP, Charles AC. Reduced threshold for cortical spreading depression in female mice. *Annals of Neurology*. 2007;61:603-6.

31. Ayata C. Spreading depression and neurovascular coupling. *Stroke; a journal of cerebral circulation*. 2013;44(6 Suppl 1):S87-9. doi: 10.1161/STROKEAHA.112.680264. PubMed PMID: 23709742.
32. Takano T, Tian GF, Peng W, Lou N, Lovatt D, Hansen AJ, Kasischke KA, Nedergaard M. Cortical spreading depression causes and coincides with tissue hypoxia. *Nature Neuroscience*. 2007;10:754-62.
33. Lauritzen M, Dreier JP, Fabricius M, Hartings JA, Graf R, Strong AJ. Clinical relevance of cortical spreading depression in neurological disorders: migraine, malignant stroke, subarachnoid and intracranial hemorrhage, and traumatic brain injury. *Journal of Cerebral Blood Flow & Metabolism*. 2011;31(1):17-35.
34. Mies G, Iijima T, Hossmann KA. Correlation between peri-infarct DC shifts and ischaemic neuronal damage in rat. *Neuroreport*. 1993;4(6):709-11. PubMed PMID: 8347812.
35. Iadecola C. Cerebral circulatory dysregulation in ischemia. In: Ginsberg MD, editor. *Cerebrovascular disease: pathophysiology, diagnosis, and management*. Malden: Blackwell Publishing; 1998. p. 319-32.
36. Girouard H, Iadecola C. Neurovascular coupling in the normal brain and in hypertension, stroke, and Alzheimer disease. *Journal of Applied Physiology*. 2006;100:318-35.
37. Paulson OB. Cerebral apoplexy (stroke): pathogenesis, pathophysiology and therapy as illustrated by regional blood flow measurements in the brain. *Stroke; a journal of cerebral circulation*. 1971;2(4):327-60. PubMed PMID: 4398838.
38. Bundo M, Inao S, Nakamura A, Kato T, Ito K, Tadokoro M, Kabeya R, Sugimoto T, Kajita Y, Yoshida J. Changes of neural activity correlate with the severity of cortical ischemia in patients with unilateral major cerebral artery occlusion. *Stroke; a journal of cerebral circulation*. 2002;33(1):61-6. PubMed PMID: 11779890.
39. Nedergaard M, Gjedde A, Diemer NH. Focal ischemia of the rat brain: autoradiographic determination of cerebral glucose utilization, glucose content, and blood flow. *Journal of cerebral blood flow and metabolism : official journal of the International Society of Cerebral Blood Flow and Metabolism*. 1986;6(4):414-24. doi: 10.1038/jcbfm.1986.74. PubMed PMID: 3733901.
40. Carmichael ST, Tatsukawa K, Katsman D, Tsuyuguchi N, Kornblum HI. Evolution of diaschisis in a focal stroke model. *Stroke; a journal of cerebral*

circulation. 2004;35(3):758-63. doi: 10.1161/01.STR.0000117235.11156.55. PubMed PMID: 14963280.

41. Liebeskind DS. Collateral circulation. *Stroke*. 2003;34:2279-84.
42. Hinman JD, Rasband MN, Carmichael ST. Remodeling of the axon initial segment after focal cortical and white matter stroke. *Stroke; a journal of cerebral circulation*. 2013;44(1):182-9. doi: 10.1161/STROKEAHA.112.668749. PubMed PMID: 23233385; PubMed Central PMCID: PMC3973016.
43. Kumagai T, Walberer M, Nakamura H, Endepols H, Sue M, Vollmar S, Adib S, Mies G, Yoshimine T, Schroeter M, Graf R. Distinct spatiotemporal patterns of spreading depolarizations during early infarct evolution: evidence from real-time imaging. *Journal of cerebral blood flow and metabolism : official journal of the International Society of Cerebral Blood Flow and Metabolism*. 2011;31(2):580-92. doi: 10.1038/jcbfm.2010.128. PubMed PMID: 20700132; PubMed Central PMCID: PMC3049513.
44. Faraci FM. Oxidative stress: the curse that underlies cerebral vascular dysfunction? *Stroke; a journal of cerebral circulation*. 2005;36(2):186-8. doi: 10.1161/01.STR.0000153067.27288.8b. PubMed PMID: 15653575.
45. Traystman RJ, Kirsch JR, Koehler RC. Oxygen radical mechanisms of brain injury following ischemia and reperfusion. *J Appl Physiol (1985)*. 1991;71(4):1185-95. PubMed PMID: 1757340.
46. Scheller MS, Tateishi A, Drummond JC, Zornow MH. The effects of sevoflurane on cerebral blood flow, cerebral metabolic rate for oxygen, intracranial pressure, and the electroencephalogram are similar to those of isoflurane in the rabbit. *Anesthesiology*. 1988;68(4):548-51. PubMed PMID: 3354892.
47. Olney JW, Labruyere J, Wang G, Wozniak DF, Price MT, Sesma MA. NMDA antagonist neurotoxicity: mechanism and prevention. *Science*. 1991;254(5037):1515-8.
48. Hernández-Cáceres J, Macías-González R, Brozek G, Bures J. Systemic ketamine blocks cortical spreading depression but does not delay the onset of terminal anoxic depolarization in rats. *Brain Research*. 1987;437(2):360-4.
49. Verhaegen M, Todd MM, Warner DS. The influence of different concentrations of volatile anesthetics on the threshold for cortical spreading depression in rats. *Brain research*. 1992;581(1):153-5. PubMed PMID: 1498665.
50. Kudo C, Nozari A, Moskowitz MA, Ayata C. The impact of anesthetics and hyperoxia on cortical spreading depression. *Exp Neurol*. 2008;212(1):201-6. doi:

10.1016/j.expneurol.2008.03.026. PubMed PMID: 18501348; PubMed Central PMCID: PMC2459317.

51. Kitahara Y, Taga K, Abe H, Shimoji K. The effects of anesthetics on cortical spreading depression elicitation and c-fos expression in rats. *J Neurosurg Anesthesiol.* 2001;13(1):26-32. PubMed PMID: 11145474.

52. Guedes RC, Barreto JM. Effect of anesthesia on the propagation of cortical spreading depression in rats. *Brazilian journal of medical and biological research* 1992;25(4):393-7.

53. Kawaguchi M, Furuya H, Patel PM. Neuroprotective effects of anesthetic agents. *Journal of Anesthesia.* 2005;19(2):150-6.

54. Hendrich KS, Kochanek PM, Melick JA, Schiding JK, Statler KD, Williams DS, Marion DW, Ho C. Cerebral perfusion during anesthesia with fentanyl, isoflurane, or pentobarbital in normal rats studied by arterial spin-labeled MRI. *Magnetic resonance in medicine : official journal of the Society of Magnetic Resonance in Medicine / Society of Magnetic Resonance in Medicine.* 2001;46(1):202-6. PubMed PMID: 11443729.

55. Cramer SC, Nelles G, Benson RR, Kaplan JD, Parker RA, Kwong KK, Kennedy DN, Finklestein SP, Rosen BR. A functional MRI study of subjects recovered from hemiparetic stroke. *Stroke; a journal of cerebral circulation.* 1997;28(12):2518-27. PubMed PMID: 9412643.

56. Austin VC, Blamire AM, Allers KA, Sharp T, Styles P, Matthews PM, Sibson NR. Confounding effects of anesthesia on functional activation in rodent brain: a study of halothane and alpha-chloralose anesthesia. *Neuroimage.* 2005;24(1):92-100. doi: 10.1016/j.neuroimage.2004.08.011. PubMed PMID: 15588600.

57. Antognini JF, Buonocore MH, Disbrow EA, Carstens E. Isoflurane anesthesia blunts cerebral responses to noxious and innocuous stimuli: a fMRI study. *Life Sci.* 1997;61(24):PL 349-54. PubMed PMID: 9399635.

58. Gehrmann J, Mies G, Bonnekoh P, Banati R, Iijima T, Kreutzberg GW, Hossmann KA. Microglial reaction in the rat cerebral cortex induced by cortical spreading depression. *Brain Pathol.* 1993;3(1):11-7. PubMed PMID: 8269080.

59. Ye X, Lian Q, Eckenhoff MF, Eckenhoff RG, Pan JZ. Differential general anesthetic effects on microglial cytokine expression. *Public Library of Science One.* 2013;8(1):e52887.

60. Wu X, Lu Y, Dong Y, Zhang G, Zhang Y, Xu Z, Culley DJ, Crosby G, Marcantonio ER, Tanzi RE, Xie Z. The inhalation anesthetic isoflurane increases

levels of proinflammatory TNF-alpha, IL-6, and IL-1beta. *Neurobiol Aging*. 2012;33(7):1364-78. doi: 10.1016/j.neurobiolaging.2010.11.002. PubMed PMID: 21190757; PubMed Central PMCID: PMC3117127.

61. Chang Y LJ, Hsieh CY, Hsiao G, Chou DS, Sheu JR. Inhibitory effects of ketamine on lipopolysaccharide-induced microglial activation. *Mediators of inflammation*. 2009;705379.

62. Patel AR, Ritzel R, McCullough LD, Liu F. Microglia and ischemic stroke: a double-edged sword. *International journal of physiology, pathophysiology and pharmacology*. 2013;5(2):73-90. PubMed PMID: 23750306; PubMed Central PMCID: PMC3669736.

63. Rosenberg GA. Matrix metalloproteinases and their multiple roles in neurodegenerative diseases. *The Lancet Neurology*. 2009;8(2):205-16. doi: 10.1016/S1474-4422(09)70016-X. PubMed PMID: 19161911.

64. Arai K, Jin G, Navaratna D, Lo EH. Brain angiogenesis in developmental and pathological processes: neurovascular injury and angiogenic recovery after stroke. *FEBS J*. 2009;276(17):4644-52. doi: 10.1111/j.1742-4658.2009.07176.x. PubMed PMID: 19664070; PubMed Central PMCID: PMC3712842.

65. Van Veluw SJ, Zwanenburg JJM, J E-L, Spliet WGM, Hendrikse J, Luijten PR, Biessels GJ. In vivo detection of cerebral cortical microinfarcts with high-resolution 7T MRI. *Journal of cerebral blood flow and metabolism*. 2012;in press. Epub December 19, 2012.

66. Matthews FE, Brayne C, Lowe J, McKeith I, Wharton SB, Ince P. Epidemiological pathology of dementia: attributable-risks at death in the Medical Research Council Cognitive Function and Ageing Study. *PLoS medicine*. 2009;6(11):e1000180. doi: 10.1371/journal.pmed.1000180. PubMed PMID: 19901977; PubMed Central PMCID: PMC2765638.

67. Smith EE, Schneider JA, Wardlaw JM, Greenberg SM. Cerebral microinfarcts: the invisible lesions. *The Lancet Neurology*. 2012;11(3):272-82. doi: 10.1016/S1474-4422(11)70307-6. PubMed PMID: 22341035; PubMed Central PMCID: PMC3359329.

68. Shih AY, Blinder P, Tsai PS, Friedman B, Stanley G, Lyden PD, Kleinfeld D. The smallest stroke: Occlusion of one penetrating vessel leads to infarction and a cognitive deficit. *Nature Neuroscience*. 2013;16:55-63.

69. Watson BD, Dietrich WD, Busto R, Wachtel MS, Ginsberg MD. Induction of reproducible brain infarction by photochemically initiated thrombosis. *Annals of Neurology*. 1985;17:497-504.

70. Shih AY, Driscoll J, Drew PJ, Friedman B, Lyden PD, Kleinfeld D, editors. Occlusion of a single penetrating arteriole is sufficient to demonstrate multiple features of stroke pathology in cerebral cortex. *Neuroscience* 2009; 2009; Chicago: Society for Neuroscience.
71. Shih AY, Nishimura N, Nguyen J, Friedman B, Lyden PD, Schaffer CB, Kleinfeld D. Optically induced occlusion of single blood vessels in rodent neocortex. *Cold Spring Harb Protoc.* 2013;2013(12):1153-60. doi: 10.1101/pdb.prot079509. PubMed PMID: 24298038.
72. Taylor ZJ, Shih AY. Targeted Occlusion of Individual Pial Vessels of Mouse Cortex. *Bio-protocol.* 2013;3(17):e897.
73. Shih AY, Drew PJ, Mateo C, Tsai PS, Kleinfeld D. A polished and reinforced thinned skull window for long-term imaging and optical manipulation of the mouse cortex. *Journal of Visualized Experiments.* 2012;Mar 7(61).
74. Nguyen Q-T, Dolnick EM, Driscoll J, Kleinfeld D. MPScope 2.0: A computer system for two-photon laser scanning microscopy with concurrent plasma-mediated ablation and electrophysiology. In: Frostig RD, editor. *Methods for In Vivo Optical Imaging*, 2nd edition. Boca Raton: CRC Press; 2009. p. 117-42.
75. Nguyen Q-T, Tsai PS, Kleinfeld D. MPScope: A versatile software suite for multiphoton microscopy. *Journal of Neuroscience Methods.* 2006;156:351-9.
76. Drew PJ, Shih AY, Kleinfeld D. Fluctuating and sensory-induced vasodynamics in rodent cortex extends arteriole capacity. *Proceedings of the National Academy of Sciences USA.* 2011;108:8473-8.
77. Bullitt E. Expression of c-fos-like protein as a marker for neuronal activity following noxious stimulation in the rat. *The Journal of comparative neurology.* 1990;296(4):517-30. doi: 10.1002/cne.902960402. PubMed PMID: 2113539.
78. Park KW, Dai HB, Comunale ME, Gopal A, Sellke FW. Dilation by isoflurane of precontracted, very small arterioles from human right atrium is mediated in part by K(+)-ATP channel opening. *Anesthesia and analgesia.* 2000;91(1):76-81. PubMed PMID: 10866890.
79. Carrera E, Tononi G. Diaschisis: past, present, future. *Brain.* 2014;137(Pt 9):2408-22. doi: 10.1093/brain/awu101. PubMed PMID: 24871646.
80. Bonilha L, Nesland T, Rorden C, Fillmore P, Ratnayake RP, Fridriksson J. Mapping remote subcortical ramifications of injury after ischemic strokes. *Behavioural neurology.* 2014;2014:215380. doi: 10.1155/2014/215380. PubMed PMID: 24868120; PubMed Central PMCID: PMC4017848.

81. Schubert D, Kotter R, Luhmann HJ, Staiger JF. Morphology, electrophysiology and functional input connectivity of pyramidal neurons characterizes a genuine layer Va in the primary somatosensory cortex. *Cerebral Cortex*. 2006;16:223-36.
82. Avermann M, Tomm C, Mateo C, Gerstner W, Petersen CC. Microcircuits of excitatory and inhibitory neurons in layer 2/3 of mouse barrel cortex. *J Neurophysiol*. 2012;107(11):3116-34. doi: 10.1152/jn.00917.2011. PubMed PMID: 22402650.
83. Garbuzova-Davis S, Rodrigues MC, Hernandez-Ontiveros DG, Tajiri N, Frisina-Deyo A, Boffeli SM, Abraham JV, Pabon M, Wagner A, Ishikawa H, Shinozuka K, Haller E, Sanberg PR, Kaneko Y, Borlongan CV. Blood-brain barrier alterations provide evidence of subacute diaschisis in an ischemic stroke rat model. *PLoS one*. 2013;8(5):e63553. doi: 10.1371/journal.pone.0063553. PubMed PMID: 23675488; PubMed Central PMCID: PMC3651135.
84. Garbuzova-Davis S, Haller E, Williams SN, Haim ED, Tajiri N, Hernandez-Ontiveros DG, Frisina-Deyo A, Boffeli SM, Sanberg PR, Borlongan CV. Compromised blood-brain barrier competence in remote brain areas in ischemic stroke rats at the chronic stage. *The Journal of comparative neurology*. 2014;522(13):3120-37. doi: 10.1002/cne.23582. PubMed PMID: 24610730; PubMed Central PMCID: PMC4107178.
85. Buchkremer-Ratzmann I, August M, Hagemann G, Witte OW. Electrophysiological transcortical diaschisis after cortical photothrombosis in rat brain. *Stroke*. 1996;27(6):1105-11.
86. Lim DH, LeDue JM, Mohajerani MH, Murphy TH. Optogenetic mapping after stroke reveals network-wide scaling of functional connections and heterogeneous recovery of the peri-infarct. *The Journal of neuroscience : the official journal of the Society for Neuroscience*. 2014;34(49):16455-66. doi: 10.1523/JNEUROSCI.3384-14.2014. PubMed PMID: 25471583.
87. Zhang S, Boyd J, Delaney KR, Murphy TH. Rapid reversible changes in dendritic spine structure *in vivo* gated by the degree of ischemia. *Journal of Neuroscience*. 2005;25:5333-228.
88. Stanimirovic D, Satoh K. Inflammatory mediators of cerebral endothelium: a role in ischemic brain inflammation. *Brain Pathol*. 2000;10(1):113-26. PubMed PMID: 10668901.
89. Helmke BP, Bremner SN, Zweifach BW, Skalak R, Schmid-Schonbein GW. Mechanisms for increased blood flow resistance due to leukocytes. *American Journal of Physiology*. 1997;273:H2884-H90. PubMed PMID: 9435628.

90. Amantea D, Nappi G, Bernardi G, Bagetta G, Corasaniti MT. Post-ischemic brain damage: pathophysiology and role of inflammatory mediators. *FEBS J.* 2009;276(1):13-26. doi: 10.1111/j.1742-4658.2008.06766.x. PubMed PMID: 19087196.
91. Jin R, Yang G, Li G. Inflammatory mechanisms in ischemic stroke: role of inflammatory cells. *Journal of leukocyte biology.* 2010;87(5):779-89. doi: 10.1189/jlb.1109766. PubMed PMID: 20130219; PubMed Central PMCID: PMC2858674.
92. Yata K, Nishimura Y, Uekawa M, Tomita Y, Suzuki N, Tanaka T, Mizoguchi A, Tomimoto H. In vivo imaging of the mouse neurovascular unit under chronic cerebral hypoperfusion. *Stroke; a journal of cerebral circulation.* 2014;45(12):3698-703. doi: 10.1161/STROKEAHA.114.005891. PubMed PMID: 25370583.
93. Carmichael ST. Cellular and molecular mechanisms of neural repair after stroke: making waves. *Annals of neurology.* 2006;59(5):735-42. doi: 10.1002/ana.20845. PubMed PMID: 16634041.
94. Carmichael ST. Themes and strategies for studying the biology of stroke recovery in the poststroke epoch. *Stroke; a journal of cerebral circulation.* 2008;39(4):1380-8. doi: 10.1161/STROKEAHA.107.499962. PubMed PMID: 18309162; PubMed Central PMCID: PMC2711539.
95. Nishimura N, Rosidi NL, Iadecola C, Schaffer CB. Limitations of collateral flow after occlusion of a single cortical penetrating arteriole. *Journal of Cerebral Blood Flow & Metabolism.* 2010;30:1914-27.
96. Maneen MJ, Hannah R, Vitullo L, DeLance N, Cipolla MJ. Peroxynitrite diminishes myogenic activity and is associated with decreased vascular smooth muscle F-actin in rat posterior cerebral arteries. *Stroke.* 2006;37(3):894-9.
97. An G, Lin TN, Liu JS, Xue JJ, He YY, Hsu CY. Expression of c-fos and c-jun family genes after focal cerebral ischemia. *Annals of neurology.* 1993;33(5):457-64. doi: 10.1002/ana.410330508. PubMed PMID: 7684582.
98. Uemura Y, Kowall NW, Moskowitz MA. Focal ischemia in rats causes time-dependent expression of c-fos protein immunoreactivity in widespread regions of ipsilateral cortex. *Brain research.* 1991;552(1):99-105. PubMed PMID: 1913186.